Dissertation

submitted to the

Combined Faculties for Natural Sciences and for Mathematics

of the Ruperto-Carola University of Heidelberg, Germany

for the degree of

Doctor of Natural Sciences

presented by

Dipl.–Phys. Stefan Spindeldreher

born in Krefeld, Germany

Oral examination: 11th of July, 2002

The Discontinuous Galerkin Method
applied on the equations of ideal relativistic hydrodynamics

Referees: **Prof. Dr. Max Camenzind**

Priv. Doz. Dr. Andreas Burkert

Zusammenfassung

Im Rahmen dieser Arbeit wurde ein Code zur numerischen Lösung der zeitabhängigen Gleichungen der relativistischen Hydrodynamik idealer Gase entwickelt. Die Erhaltungsgleichungen wurden mit Hilfe der Diskontinuierlichen Galerkin Methode (DGM) diskretisiert, welche eine Erweiterung der Finiten Element Methode (FEM) ist. Im Gegensatz zu den klassischen Finiten Element Methoden ist die DG Methode auch im Falle Advektions-dominierter Probleme numerisch stabil. Die vorteilhafte Eigenschaft der FE Methoden hoher numerischer Genauigkeit bei einer räumlichen Diskretisierung mittels unstrukturierte Gitter bleibt erhalten. Eine höhere formale räumliche Ordnung kann durch die Wahl einer entsprechenden Finiten Element Basis leicht erreicht werden. Desweiteren ist aufgrund der diskontinuierlichen Basis eine effiziente Parallelisierung möglich. Die zeitliche Integration wird mittels eines mehrstufigen expliziten Runge-Kutta-Verfahrens durchgeführt. Der Code bestand erfolgreich die ein- und zweidimensionalen Standardtestprobleme der Newtonischen und relativistischen Hydrodynamik. Es zeigte sich, dass die effektive Auflösung der DG Methode vergleichbar mit der typischen Auflösung moderner High Resolution Shock Capturing (HRSC) Methoden ist. Der Code wurde auf das astrophysikalisch interessante Problem der Propagation relativistischer Jets angewendet. Desweiteren wurde die zeitliche Entwicklung einer relativistischen Akkretionsscheibe eines nichtrotierenden Schwarzen Lochs simuliert.

Summary

To solve numerically the problems of ideal relativistic hydrodynamics we have developed a high-order accurate and time-explicite code. For the spatial discretisation we use the Discontinuous Galerkin Method (DGM), which is a sub-class of the Finite Element Methods (FEM). The DG methods are numerically stable for advection-dominated problems and a high-order of spatial accuracy is reachable, even by using unstructured meshes for the discretisation of a computational domain. A higher formal accuracy is easily achieved by using a higher-order Finite Element basis. Further, a efficient parallelisation of the DG method is possible, due to their compact form. This code was able to solve the standard test-problems of the Newtonian and relativistic hydrodynamics in one and two dimensions with high accuracy. The effective resolution reached in the computation is comparable to that of the modern High Resolution Shock Capturing (HRSC) methods. In addition, we applied the code to astrophysical problems of interest, a jet propagating in a homogeneous media and relativistic accretion disc of Black Holes.

Contents

Chapter 1

Introduction

1.1 Simulation, a laboratory for astrophysics

The question arises why simulations are required in astrophysics? In astrophysics the situation occurs that the typical phenomena of interest, like the formation and evolution of stars and galaxies, as well accretion processes and their connection to the formation of jets, are located at high distances and also the typical evolution time scales could be large compared to the human life time. Further, the processes of these phenomena may involve extreme physical conditions which are not possible to study by experiments on earth. The situation is further complicated by the fact, that the involved physical processes of these phenomena, may occur deep inside of the region where the measurable radiation is emitted, and therefore, we can only get a indirect evidence of these involved processes by observations. These are the main differences to most fields in physics, where a direct experimental falsification of a theoretical hypothesis is possible. On the other hand, to make the astrophysical problems analytically solvable in a theoretical approach, the complex phenomena have to be simplified, by linearising nonlinear problems or reducing the degrees of freedom by introducing new parameters. This restricts the solution to a small class of the possible phenomena evolved in nature. By solving the problems in a numerical approach, less simplifications of the models are needed, although not completely avoidable, since one is restricted by the nowaday available computer resources, but a larger physical range of complex phenomena is possible to investigate than in the analytical way. Further, simulations can tell us how good are the assumption of the analytical model. In no way an analytical understanding is overcome by the numerical, but the latter one can help. In addition, analytical solutions are needed for the validation and calibration of a new developed code, to get an estimate of the reached numerical accuracy. After the validation of the code, one has a laboratory on the table, to compare the theoretical models with observations. The observational evidence of phenomena, like Active Galactic Nuclei (AGN) and their outflows (jets), as

well the existence of micro-Quasars in our galaxy, where relativistic effects are not-negligible, implies to solve the full relativistic equations of hydrodynamics. To mimic the relativistic effects of curved spacetime of Black Holes the commonly used approach was to replace the Newtonian gravitation potential $\Phi \propto M/r$ by the Paczyńsky-Wiita [47] potential $\Phi \propto M/(r-2M)$ for non rotating Black Holes or by the Pseudo-Kerr-Potential $\Phi = 1 + \frac{M}{r-r_0} + \frac{1}{2}\omega^2 r^2$, introduced by Chakrabarti and Khanna [10] and to solve the nonrelativistic equations of hydrodynamics. A second commonly approach is the solving of the Post-Newtonian equations. Both of these approaches include the disadvantage that the contribution of the internal energy to the effective inertia is neglected, which is a bad assumption for relativistic hot fluids, as well there exist no limiting of the flow velocities by the speed of light.

Nowaday several codes are available, which are using a variety of numerical schemes for the different astrophysical problems. In this work, we will restrict to the codes solving the equations of relativistic hydrodynamics. To do this, in numerical relativity, the commonly used schemes are high order Finite Difference (FD) and Finite Volume (FV) methods, as well there is a application of the Smoothed Particle Hydrodynamics (SPH) for this problems. An introduction into the field of numerical hydrodynamics in special relativity is given in the review article of Martí and Müller [39] and in the review of Font [20] for the general relativistic case. Relativistic hydrodynamics has been applied essentially for the two following astrophysical problems.

Relativistic accretion disc simulations. The first two-dimensional axisymmetric and time-dependent simulations of accretion discs around Black Holes were done by the pioneering work of Hawley, Smarr & Wilson [22, 23]. The relativistic equations of hydrodynamic were solved in the non-conservative formulation of Wilson [60], where the gradient of the pressure ∇p was evaluated as a force term. They studied the development and evolution of non-linear instabilities of angular momentum pressure supported tori. The code uses a second order Finite Difference scheme on a staggered grid, including a variety of schemes for the advection terms. Discontinuities were stabilised by an artificial viscosity scheme. An extension to three-dimension was done by Hawley [21], where the evolution of non-axisymmetric instabilities of constant angular momentum accretion tori was studied.

The problem of thick accretion discs was further studied by Igumenshchev and Belodorov [26], using also the Wilson formulation of relativistic hydrodynamics. As initial conditions they used the analytical solution of a constant angular momentum pressure-supported tori. The rotating tori are separated from the black hole by a potential barrier of height ΔW. If $\Delta W > 0$ the torus is unstable to any perturbation. The authors studied the dynamics for different potential barriers $\Delta W > 0$ and black hole spin parameter $a = -0.9, 0, 0.9$. In these simulations

the flow was only irrotational in the vicinity of the potential barrier. At larger disc radii quasi-periodical vortex motions of the fluid were developed. Their procedure for the advection terms based on a upwind scheme, where the Piecewise Parabolic Method (PPM) of Colella and Woodward [15] was used to evaluate the fluxes. Their scheme need no artificial viscosity to stabilise discontinuities.

The structure and dynamics of magneto-hydrodynamical viscous accretion discs was studied by Yokosava [63, 62]. The viscosity based on the α viscosity parametrisation of Shakura & Sunyaev [52]. Yokosava also used Wilson's formulation. For solving the hydrodynamical part of the MHD equations the code uses a Flux-Corrected Transport (FCT) scheme [8] , whereby the magnetic induction equation was solved using the constrained transport method [19].

The time-dependent problem of magneto-hydrodynamical driven jet formation from relativistic accretion discs in the Kerr space was investigated by Koide, Shibata & Kudoh [29, 30]. In their simulations, a two-component magnetised sub-relativistic jet evolves, which is accelerate from the accretion disc. A fast inner jet component, driven by high pressure region appearing in the vicinity of the marginal stable radius, is embedded by a low velocity component, driven by magnetic forces. The highest poloidal velocity of the outflow $0.4c$ was reached for a counter-rotating disc (relative to the rotation of the black hole). In the co-rotating case only a jet velocity of $0.3c$ was reached. In their simulations, a collimation of the jet was not possible to achieve, since the spatial scale of the computational domain was to small and the evolution time was to short. The equations of relativistic magnetohydrodynamics were discretised in conservative form. The fluxes are computed by a simplified Total Variation Diminishing (TVD) scheme, where only the largest eigenvalue λ_{max} of the flux Jacobian $\mathbf{A} = \partial\mathbf{F}(\mathbf{U})/\partial\mathbf{U}$, is needed.

Relativistic jet simulations. The first simulation of the propagation of relativistic jets was done by van Putten [57, 58], who used a pseudo spectral scheme for solving the equations of relativistic magnetohydrodynamics. In his first work a jet in slab geometry with beam Lorentz factor $W_b = 3.25$ was studied. The jet propagation was computed to seven jet radii. In 1994 the first long scale runs of axisymmetric jets, were performed by Martí and Müller [38] and Duncan and Hughes [18]. In these simulations they studied the propagation of hot relativistic jets, i.e. jets with a low beam Mach number. The code of [38] includes a High Resolution Shock Capturing (HRSC) scheme, which based on an approximate Riemann solver. Duncan and Hughes [18] also studied the long term dynamics and morphology of relativistic hot jets. Their code also includes a Godunov-type scheme based on an approximate Riemann solver. In addition, they use an Adaptive Mesh Refinement (AMR) method to reduce the computational effort. Both groups derived similar results of the morphology and propagation properties of hot jets. Typical relativistic hot jets achieve a high propagation efficiency. The beam and the surrounding shocked gas are nearly in pressure equilibrium and no

dominant cocoon of back-flowing jet matter is developed. Since in the beam no strong internal shocks are excited, the jet propagates nearly in a one-dimensional fashion. Komissarov and Falle [33, 34] developed also a code for solving the equations of relativistic hydrodynamics. Their code is based on an approximate Riemann solver for the linearised equations of the primitive variables.

To study non-axisymmetric instabilities, Hughes et al. [25] and Aloy et al. [1] extend their codes to three dimensions. Hughes and coworker studied in their work a jet propagating through an ambient medium, including initially a density gradient. This was computed for different angles of the density gradient relatively to the jet axis. Further they studied the propagation properties of a precessing jet. The simulation of three dimensional MHD jets started by the work of Koide et al. [28] and Nichikawa et al. [44, 45]. In their computations a fluid was injected into an ambient medium, which contains a strong ordered magnetic field.

Motivation for this work. This work was motivated, by the work of Khanna and Camenzind [27], where the formation of disc dynamos in the stationary Kerr metric of rotating Black Holes was analysed in the 3+1 split of spacetime. They solved numerically the time-dependent relativistic dynamo equations in a hydro-kinematic approach, where the velocity fields were analytically given, by using a Finite Element Method. Since this approach was kinematical, the back reaction of the evolving electromagnetic fields onto the matter was neglected. To ensure a coupling between matter and the dynamo, the idea was to develop a relativistic magneto-hydro code to solve the equations in a stationary background metric. The first step to this challenging problem of relativistic computation was to develop a code for the ideal relativistic hydrodynamics in the one-fluid approach. By neglecting self-gravity of the fluid, only the conservation laws of hydrodynamics, living in a stationary background spacetime, have to be computed. This assumption seems to be reasonable in the case of accretion onto compact objects like Neutron stars and Black Holes. In the vicinity of these objects the mass of the disc M_{Disc} is negligible compared to the mass of the compact object, $M_{C.O} \gg M_{Disc}$. This also holds for the problem of relativistic jet propagation, where the kinetic and internal energy density of the fluid are much larger compared to the energy density of self-gravity. The code presented in this work is able to solve the equations of the ideal relativistic hydrodynamics in Cartesian, cylindrical and spherical coordinates including the Schwarzschild metric in two dimensions. The scheme is based on the time explicite Runge-Kutta Discontinuous Galerkin Method (RKDGM) introduced by Cockburn and Shu [13] for the Newtonian ideal hydrodynamics. Finite Element Methods play a rather exotic part in the computational astrophysics community; therefore the DGM method is explicitly discussed in chapter 2 for conservation laws. Since the DG method is a Finite Element method, the advantageous properties of easy increasing the order of approximation and high accuracy on unstructured meshes is preserved.

In chapter 3 the test problems solved by the code are shown. Also there are some applications on astrophysical problems, like the relativistic jet propagation in cylindrical coordinates and a Keplerian disc in the Schwarzschild metric, of a non rotating Black Hole, shown in chapter 4.

1.2 The reliability of hydrodynamical approximation

The reliability of the macroscopical approach of approximate a gas or plasma by a compressible continuous fluid depends on the involved microscopical physics of the single particles and their interactions. The hydrodynamical approach is reliable if the microscopic collisional mean free path length λ_p of a particle is negligibly small compared to characteristic length scales of the investigated system L, or, in other words, the microscopic collision time τ has to be small compared to the dynamical time t of the problem. Further, the forces between the particles have to saturate over small scales, if not collective effects must to be taken into account like self-gravity, electro-magnetic mean fields and diffusion.

1.3 Equations of ideal relativistic hydrodynamics

The dynamics of a perfect fluid moving with the 4-velocity u^μ in a general spacetime, with 4-metric $g_{\mu\nu}$, is determined by the local conservation laws of the hydrodynamics and Einstein's equations. In the following we use the convention of Misner, Thorne and Wheeler [43] for the normalisation of the 4-velocity, $g_{\mu\nu}u^\mu u^\nu = -1$. We use units where the constant of gravitation G and the vacuum speed of light c are $G = c = 1$. The velocities are measured in units of the light speed. The equations of the relativistic hydrodynamics are given by the equation of local particle conservation

$$\nabla_\mu \rho^\mu = 0, \tag{1.1}$$

where ∇_μ is the covariant derivation, and by the local conservation of the energy-momentum

$$\nabla_\mu T^{\mu\nu} = 0\ , \tag{1.2}$$

where $\rho^\mu = \rho u^\mu$ is the four particle current and the energy-momentum tensor of a relativistic perfect gas is given by $T^{\mu\nu} = \rho h u^\mu u^\nu + p g^{\mu\nu}$. The rest-mass density ρ and relativistic specific enthalpy $h = 1 + \epsilon + p/\rho$ are defined in the rest frame of the fluid. The system is closed by an equation of state $p = p(\rho, \epsilon)$, which is for ideal compressible fluids given by $p = (\gamma - 1)\rho\epsilon$. In general, the metric of spacetime is coupled by the Einstein's equations

$$G_{\mu\nu} = 8\pi T_{\mu\nu} \tag{1.3}$$

to the energy-momentum of the fluid. By the assumption of negligible contribution of the fluids energy-momentum to the energy-momentum given for a compact object $G_{\mu\nu} \approx 8\pi T^{c.o.}_{\mu\nu}$, the metric is decoupled from the flow. The dynamics of a perfect fluid is then determined by the background metric, the initial and boundary conditions of the flow and the conservation laws (1.1), (1.2). The special case of a axisymmetric, $\partial_\phi g_{\mu\nu} = 0$, and stationary, $\partial_t g_{\mu\nu} = 0$, solutions of Einstein's equations, like the Kerr metric for rotating Black Holes and the Schwarzschild solution for the non-rotating case, leads to the existence of the Killing fields ${\xi_{(t)}}^\mu = \partial_t$ and ${\xi_{(\phi)}}^\mu = \partial_\phi$ and the presence of global conserved quantities. The line element of these types of spacetimes can always be written in the form

$$ds^2 = g_{tt}dtdt + 2g_{t\phi}dtd\phi + g_{\phi\phi}d\phi d\phi + g_{AB}dx^A dx^B. \tag{1.4}$$

The metric coefficient $g_{\mu\nu}$ are only functions of the coordinates x^A, x^B, with the connection to the Killing fields ${\xi_{(t)}}_\mu {\xi_{(t)}}^\mu = g_{tt}$, ${\xi_{(t)}}_\mu {\xi_{(\phi)}}^\mu = g_{t\phi}$ and ${\xi_{(\phi)}}_\mu {\xi_{(\phi)}}^\mu = g_{\phi\phi}$. By contracting the energy-momentum tensor by the Killing fields one gets the energy current

$$e^\mu = T^\mu_\nu {\xi_{(t)}}^\nu \tag{1.5}$$

and momentum current

$$p^\mu = -T^\mu_\nu {\xi_{(\phi)}}^\nu \tag{1.6}$$

with the properties

$$\nabla_\mu e^\mu = 0 \text{ and } \nabla_\mu p^\mu = 0\ . \tag{1.7}$$

By using $u_0 = u_\mu {\xi_{(t)}}^\mu$ and $u_\phi = u_\mu {\xi_{(\phi)}}^\mu$, this leads to the advection equations of energy

$$\rho^\mu \nabla_\mu (u_0 h) = 0 \tag{1.8}$$

and angular momentum

$$\rho^\mu \nabla_\mu (u_\phi h) = 0 \tag{1.9}$$

therefore the quantities $E = hu_0$ and $L = hu_\phi$ are conserved along the stream lines of the flow. Additionally, from these properties it follows that the specific angular momentum $l = u_\phi / u_0$ is also a conserved quantity advected by the flow.

1.4 The ADM formalism or splitting spacetime into space and time

In the ADM formalism or the 3+1 split of spacetime, introduced by Arnowitt, Deser & Misner [2], the spacetime is foliated into slices of nonintersecting spacelike hypersurfaces Σ_t. The position of an event e_t in the hypersurfaces Σ_t and the time advanced position of the event e_{t+dt} in Σ_{t+dt} are connected by the lapse function α which describes the rate of advance of time along a timelike unit vector orthogonal to the hypersurface Σ_t. The spacelike shift vector β^i describes

the motion of the coordinates of an event in Σ_t to the time advanced new position in the hypersurface Σ_{t+dt}. From this choice, the line element is then split into

$$ds^2 = -\alpha^2 dt^2 + \gamma_{ij}(dx^i + \beta^i dt)(dx^j + \beta^j dt) \; , \tag{1.10}$$

where γ_{ij} is the three-metric introduced on each spacelike hypersurface. The connection to the corresponding coefficients $g_{\mu\nu}$ of the 4-metric are therefore

$$\begin{bmatrix} g_{tt} & g_{tj} \\ g_{it} & g_{ij} \end{bmatrix} = \begin{bmatrix} (\beta_k \beta^k - \alpha^2) & \beta_j \\ \beta_i & \gamma_{ij} \end{bmatrix} \; .$$

The generalisation of a Newtonian Euler observer, in the 3+1 split of spacetime, is given by an observer with 4-velocity $w^\mu = (1, -\beta^i)/\alpha$, who lives in general in an accelerated frame. The 3-velocity v^i of a fluid element in Σ_t, measured in the frame of the observers, follows from the projection of the fluid's 4-velocity u^μ orthogonal to the 4-velocity w^μ of the observer. Defining the projection operator $P_{\mu\nu} = g_{\mu\nu} + w_\mu w_\nu$, the spacelike component of the fluid's 4-velocity in the observer frame is given by

$$W v^\mu = P^\mu_\nu u^\nu = u^\mu + \beta^\mu u^t \; ,$$

where $W = \alpha u^t = 1/\sqrt{1 - \gamma_{ij} v^i v^j}$ is the Lorentz factor of the fluid defined by the observers. The density D, energy E and the three momenta M_i of the fluid, measured in the frame of these observers follow from the contraction of the 4-density current ρ^μ with the observer's 4-velocity

$$D = w_\mu \rho^\mu = \rho W \tag{1.11}$$

and energy density by parallel projection, to the observers 4-velocity, of the 4-energy-momentum current $w_\nu T^{\mu\nu}$

$$E = w_\mu w_\nu T^{\mu\nu} = \rho h W^2 - p \tag{1.12}$$

The fluid momenta are the orthogonal components of the 4-energy-momentum current

$$M_\mu = P_{\mu\lambda} w_\nu T^{\lambda\nu} = \rho h W^2 v_i \; . \tag{1.13}$$

Since M_μ is orthogonal to w_μ, only the spatial coefficients of the momenta are not vanishing, $M_\mu = (0, M_i)$. Additionally, the equation of local energy conservation, measured in the frame of an observer with four velocity w_μ, follows from the projection of the divergence ∇T of the energy-momentum tensor parallel to the observer's 4-velocity w^μ

$$w_\mu \nabla_\nu T^{\mu\nu} = 0 \; , \tag{1.14}$$

where the equations of local momentum conservation are recovered by projection of the divergence of T perpendicular to the four-velocity of the observer.

$$P_{\mu\lambda} \nabla_\nu T^{\lambda\nu} = 0 \; . \tag{1.15}$$

Since the continuity equation

$$\nabla_\nu \rho^\nu = 0 \tag{1.16}$$

is scalar-like no additional projection is needed. Following Banyuls et al. [4] we introduce the vector of conservative variables

$$\mathbf{U}(\mathbf{w}) = (D, M_i, E) = \left(\rho W, \rho h W^2 v_i, \rho h W^2 - p\right) \ , \tag{1.17}$$

where D, M_i, E are the density, the three-momenta and energy of the fluid measured in the frames of the fiducial observers. By the definition of the vectors of the corresponding fluxes

$$\mathbf{F}^k(\mathbf{w}) = \begin{pmatrix} D(v^k - \frac{1}{\alpha}\beta^k) \\ M_i(v^k - \frac{1}{\alpha}\beta^k) + p\delta_i^k \\ E(v^k - \frac{1}{\alpha}\beta^k) + pv^k \end{pmatrix}, \tag{1.18}$$

it is possible to formulate the system of nonlinear equations of a perfect relativistic fluid, in a stationary spacetime, in a first order conservative hyperbolic form

$$\partial_t \sqrt{\gamma}\mathbf{U}(\mathbf{w}) + \partial_k \sqrt{-g}\mathbf{F}^k(\mathbf{w}) = \sqrt{-g}\mathbf{S}(\mathbf{w}), \tag{1.19}$$

where $\sqrt{-g} = \alpha\sqrt{\gamma}$ is determinant of 4-metric and $\sqrt{\gamma}$ the corresponding determinant of the 3-metric γ_{ij}. The vector of source terms

$$\mathbf{S}(\mathbf{w}) = \begin{pmatrix} 0 \\ (\partial_\mu g_{\nu i} - \Gamma^\lambda_{\nu\mu} g_{\lambda i}) T^{\mu\nu} \\ \alpha(T^{\mu 0}\partial_\mu \ln\alpha - \Gamma^0_{\mu\nu} T^{\mu\nu}) \end{pmatrix} \tag{1.20}$$

includes only functions of the metric coefficients, their derivatives

$$\Gamma^\lambda_{\mu\nu} = \frac{1}{2} g^{\lambda\delta}(\partial_\nu g_{\delta\mu} + \partial_\mu g_{\delta\nu} - \partial_\delta g_{\mu\nu})$$

and algebraic functions of the primitive variables $\mathbf{w} = (\rho, v_i, p)$, i.e. no derivatives of the conserved quantities $\mathbf{U}$ and primitive variables $\mathbf{w}$ are present in the source terms. This conservative formulation, Eq. (1.20), of the equations of relativistic hydrodynamics is advantageous for problems involving discontinuities, like shocks and contact discontinuities, due to the application of modern schemes developed for hyperbolic conservation laws. Since in the energy E the rest-mass energy ρW^2 is included, numerical problems are arising if the internal energy is only a small fraction of E. Therefore, instead of solving the conservation law for E we solve the equation for the conservative variable $\tau = E - D$, like Martí et al. [38]. The vector of the conservative variables evolved in time is then given by $\mathbf{U} = (D, M_i, \tau)$.

It must be noted here, that the recovering of the primitive variables $\mathbf{w} = (\rho, v_i, p)$ from the conserved ones, in the case of the ideal relativistic hydrodynamics, is not possible in a direct way, since the primitives are nonlinear functions

of the conserved ones and a closed formulation is not possible. To solve these nonlinear equations the iterative Newton-Raphson method is used. The explicite scheme is discussed in appendix B. In contrast to this, in the case of Newtonian hydrodynamics, the primitive variables

$$\mathbf{w} = \begin{pmatrix} \rho \\ v_i \\ p \end{pmatrix} = \begin{pmatrix} D \\ M_i/D \\ (\gamma-1)\left(E - M_i M^i/(2D)\right) \end{pmatrix} \tag{1.21}$$

are easily recovered from the conserved quantities (D, M_i, E). The iterative recovering of the primitive variables, which are needed for the evaluation of the fluxes and source terms, makes the computation of relativistic hydrodynamics more time consuming than their Newtonian counterpart.

Observers in a stationary axisymmetric spacetime: In the case of a stationary and axisymmetric spacetime, like the Kerr metric, the shift vector β_i has only a toroidal component β_ϕ and in the Schwarzschild metric the shift vector disappears, if the Boyer-Lindquist coordinates (t, r, θ, ϕ) are introduced. In this type of spacetime it is possible to introduce a family of distinguished observes, which are static in r and θ and do not rotate relatively to free-falling test particles dropped initially at infinity with zero angular momentum. These observers have a 4-velocity $w^\mu = (1, 0, 0, -\beta^\phi)/\alpha$ and called Zero Angular Momentum Observers (ZAMOs) or Bardeen observers. Therefore the ZAMOs are at rest in the poloidal coordinates (r, θ), with rotation frequency β^ϕ relatively to a stationary observer at infinity. This choice of observers makes it possible that the 3-metric γ_{ij} is stationary and diagonal, with the line element given by:

$$ds^2 = -(\alpha^2 - \beta_\phi \beta^\phi)dt^2 + 2\beta_\phi dt d\phi + \gamma_{ij} dx^i dx^j \ . \tag{1.22}$$

Here the lapse function is

$$\alpha = \frac{\rho}{\Sigma}\sqrt{\Delta} \ , \tag{1.23}$$

the components of the shift vector are

$$\beta^r = \beta^\theta = 0 \ , \beta^\phi = -\omega = \frac{2aMr}{\Sigma^2}, \tag{1.24}$$

and the coefficients of the 3-metric are given by

$$\gamma_{rr} = \frac{\rho^2}{\Delta}, \ \ \gamma_{\theta\theta} = \rho^2, \ \ \gamma_{\phi\phi} = \tilde{\omega}^2 \text{ and } \gamma_{ij} = 0 \text{ for } i \neq j \tag{1.25}$$

with definitions

$$a \equiv \frac{J}{M}, \ \ \Delta \equiv r^2 - 2Mr + a^2, \ \ \rho^2 \equiv r^2 + a^2 \cos^2\theta \tag{1.26}$$

$$\Sigma^2 \equiv (r^2 + a^2)^2 - a^2 \sin^2\theta, \quad \tilde{\omega} \equiv \frac{\Sigma}{\rho} \sin\theta \ . \tag{1.27}$$

M is the irreducible mass and J the angular momentum of the rotating Black Hole. The event horizon is located, where the lapse function is zero, $\alpha = 0$, and therefore $r_h = M + \sqrt{M^2 - a^2}$.

A disadvantage, using this type of observers in numerical relativity, is the presence of a coordinate singularity at the event horizon r_h, leading to a divergence of the conservative variables $\mathbf{U} = (D, M_i, \tau)$. Since this singularity at the horizon is not physical, it is possible to remove it by choosing a set of appropriate coordinates. This reformulation was introduced by Papadopoulos and Font [48] for the wind accretion problem onto rotating Black Holes. In their computations of wind accretion, it was possible to locate the inner numerical boundary inside the horizon.

1.5 The characteristics of hyperbolic conservation laws

A typical characteristic of hyperbolic conservation laws is the existence of a maximum speed of information exchange, in other words the hyperbolic equations are causal. Therefore, the domain of influence of an event, after advancing in time, is limited by the maximum characteristic speed involved in the problem. These characteristic speeds λ_p and the their corresponding waves ω_p are recovered from a spectral decomposition of the fluxes. An introduction in this field is given by LeVeque [36]. A nonlinear system of conservation laws

$$\partial_t \mathbf{U} + \nabla_k \mathbf{F}^k(\mathbf{U}) = 0 \tag{1.28}$$

is linearised by

$$\partial_t \mathbf{U} + \mathbf{A}^k \nabla_k \mathbf{U} = 0 \tag{1.29}$$

where

$$\mathbf{A}^k = \partial \mathbf{F}^k / \partial \mathbf{U} \tag{1.30}$$

is the Jacobian of the fluxes. The system is called hyperbolic, if the flux Jacobian is diagonalisable with real eigenvalues λ_p, i.e. there exists the decomposition

$$\mathbf{A} = \mathbf{R}\mathbf{\Lambda}\mathbf{R}^{-1} \ , \tag{1.31}$$

where

$$\mathbf{\Lambda} = \mathrm{diag}(\lambda_1, ..., \lambda_p) \tag{1.32}$$

is the diagonal matrix of real eigenvalues and $\mathbf{R} = (\mathbf{r}_1, ..., \mathbf{r}_m)$, $\mathbf{R}^{-1} = (\mathbf{l}_1, ..., \mathbf{l}_m)$ are the matrices of the corresponding right and left eigenvectors, $\mathbf{r}_p$, and $\mathbf{l}_p$. In the absence of discontinuities, the right eigenvectors are locally small amplitude

perturbations of the waves ω_p moving with the characteristic wave speeds λ_p. The characteristic variables are recovered from

$$\omega = \mathbf{R}^{-1}\mathbf{U} \tag{1.33}$$

and the linearised system of equations (1.29) is after transformation

$$\partial_t \omega + \Lambda^k \nabla_k \omega = 0 \tag{1.34}$$

decoupled into m scalar equations.

Linear hyperbolic system: Now we restrict ourselves to a linear, $\partial\mathbf{\Lambda}/\partial\mathbf{U} = 0$, one-dimensional problem with wave speeds λ_p constant in time and space. The solution for each characteristic variable, at the time t, is then given by

$$\omega_p(x,t) = \omega_p(x - \lambda_p t, 0) \text{ for } t \geq 0 \ ,$$

where $\omega_p(x,0) = \mathbf{R}^{-1}\mathbf{U}(x,0)$ is the initial state of the pth characteristic variable. This is a typical causal solution, since the domain of influence d_p at time t for an event at $(x_0, t = 0)$ is $d_p \in [x_0, x_0 - \lambda_p t]$ and discontinuities in the pth characteristic variables move with the corresponding wave speed λ_p.

Nonlinear hyperbolic system: A system is nonlinear if the wave speeds λ_p are functions of state vector $\mathbf{U}$, i.e.,

$$\frac{\partial \lambda_p}{\partial \mathbf{U}} \mathbf{r}_p \neq 0 \ \text{ for all } \mathbf{U}, \tag{1.35}$$

where r_p is the right eigenvector of the pth wave. These systems including the phenomena of wave breaking, the evolving of discontinuities, in a finite time, even if the initial states are smooth functions in space. The eigenvalues of the Newtonian Euler equations of a perfect compressible gas in one dimension are

$$\lambda_p = \begin{cases} \lambda_- = v - c \\ \lambda_0 = v \\ \lambda_+ = v + c, \end{cases} \tag{1.36}$$

where v is the local velocity of the fluid and c is the local sound speed. The characteristic speeds λ_-, λ_+ are the propagation speeds of the acoustic waves of the fluid, which moves with the velocity v relatively to the laboratory frame. The contact discontinuities in the characteristic variable ω_0 are transported with the characteristic speed $\lambda_0 = v$, i.e. the local velocity of the fluid. In the frame moving with the fluid velocity v we see that λ_- describes a left going acoustic wave, where λ_+ is the right going counterpart. The characteristic speeds of the relativistic conservation laws are explicitely given in appendix A.

Now we look at the characteristic speed in the vicinity of point at $x = x_0 + dx$. Here we define the characteristic speeds as: $\lambda_p^L(x \to x_0)$ and $\lambda_p^R(x \leftarrow x_0)$. A shock evolves in the characteristic variable ω_p if $\lambda_p^L \lambda_p^R < 0$ and $\lambda_p^L > 0$. A rarefaction of ω_p is evolving if $\lambda_p^L \lambda_p^R < 0$ and $\lambda_p^L < 0$.

To solve the nonlinear hyperbolic equation locally at a point x_0 in one dimension one starts from a initial value problem defined by the two conditions $U_L = U(x \to x_0)$, $U_R = U(x_0 \leftarrow x)$ at both sides of x_0, separated by a discontinuity. The corresponding initial states of the primitive variables are $w_L = (\rho_L, v_L, p_L)$ and $w_R = (\rho_R, v_R, p_R)$. This initial two state problem for a perfect gas, if $v_L = v_R = 0$, is called the Riemann problem, which is analytically solvable if initially only two constant states exist in the domain of interest. The analytic solution for the relativistic Riemann problem is given in Martí and Müller [38]. Numerical methods based on Riemann solvers use the Riemann solution. The two initial states U_L, U_R are then defined at both sides of the interface $\Gamma_{L,R}$ of two connecting computational sub-domains Ω_L, Ω_R. After solving the local Riemann problem at the interface $\Gamma_{L,R}$, the new states U_L^*, U_R^* are derived in the left and right sub-domains.

Chapter 2

The Discontinuous Galerkin Method

For solving numerical the problems of hydrodynamics (HD) and magnetohydrodynamics (MHD), where advection plays an important part, stable, accurate and efficient methods have to be applied. High accuracy is needed, since the numerical solution depends strongly on the resolution of the occurring physical discontinuities, of purely convective nonlinear problems, where a rich and complicated flow structure is developed. In addition using high order accurate schemes make it possible to use a lower grid resolution to resolve these structures and, therefore, these schemes are more computational efficient for the solving of multi-dimensional problems. The remarkable development of High Resolution Finite Difference (HRFD) and Finite Volume (HRFV) methods for nonlinear hyperbolic conservation laws, by applying of suitably defined numerical fluxes and slope limiters, include these properties. Therefore, the question arises, why using a Finite Element Method? Finite Element methods (FEM), like the Continuous Galerkin method (CGM), are able to solve most types of partial differential equations on unstructured grids and complicated computational domains with a high accuracy and a large convergence rate towards the true solution, depending on the applied order of finite element space. Unfortunately, this is not the case for problems where convection plays an important role, since a local conservation of the conserved quantities is not guaranteed and at discontinuities the FE methods become unstable.

The development of the Discontinuous Galerkin Method (DGM), introduced in 1973 by Reed and Hill [50] for the neutron transport problem, and further developed by several researchers in the nineties, overcome these difficulties, when applying the Finite Element schemes on advection dominated problems. Nowaday, several DG methods have been developed and analysed for solving the Newtonian Euler, Navier-Stokes, MHD and Maxwell equations. An overview of these schemes is given in the Lecture Notes of Cockburn, Karniadakis and Shu [12]. Due to their finite element nature, the DG methods are not very sensitive to the struc-

ture of the grid and the formal order of accuracy depends on the degree of used approximating polynomials if the solution of the problem changes smoothly in the computational domain. Applying the DG method to these nonlinear problems, the resulting system of ordinary differential equations is compact and independent of the order of space approximation, since only the connecting sub-domains are coupled by the suitably defined numerical fluxes. This property makes the DG method very efficient for parallel computing as well as for using implicit schemes. Since space discontinues basis functions are used, the advantageous schemes, for solving the nonlinear conservation laws, of the High Resolution Finite Volume methods, like slope limiter and numerical flux construction are available for the DG method. In the following sections, the explicite Runge-Kutta DG method, developed by Cockburn and Shu [13], is reviewed and applied onto the system of relativistic Euler equations.

2.1 Space discretisation

Given is a system of equations in the conservative form

$$\partial_t \mathbf{U} + \partial_k \mathbf{F}^k (\mathbf{U}) = \mathbf{S} (\mathbf{U}) \text{ in } (\mathbf{x}, t) \in \Omega \times (0, T) \tag{2.1}$$

where Ω is the bounded domain in $I\!R^d$ with boundary conditions

$$\mathbf{U} = \gamma (\mathbf{x}, t) \ ,$$

$$\partial \mathbf{U} = \partial \gamma (\mathbf{x}, t) \text{ at } \partial\Omega$$

and initial conditions

$$\mathbf{U}_0 = \mathbf{U} (\mathbf{x}, 0) \text{ at } t = 0.$$

The main difference between the FV and DG methods is the way of space discretisation. Finite volume methods achieve higher order space accuracy by the involvement of more ambient node values U_I to construct the fluxes $F_I = F (U_{I-N}, ..., U_I, ..., U_{I+N})$ at the cell interfaces. These enlarged domains of influence are difficult to implement unstructured meshes and limit a efficient implementation on parallel computer. In contrast, by using the DG Method, the computational domain Ω is subdivided into $1, \ldots, N$ sub-domains Ω_E. In each sub-domain Ω_E the solution for $U (\mathbf{x}, t)$ is approximated by a set of discontinuous basis functions $\Phi_E(\mathbf{x}) = \left[\phi_1(\mathbf{x}), \ldots, \phi_{n(p)}(\mathbf{x})\right]$ of polynomial order p, with the property

$$\int_\Omega \Phi_A \Phi_E^T d\Omega = \delta_{AE} \int_{\Omega_A} \Phi_A \Phi_E^T d\Omega \ , \tag{2.2}$$

where $\delta_{AB} = 1$ for $A = B$ and equal zero otherwise. Due to this property, it is possible to use different degrees of order $p = p(\Omega_E)$ in each sub-domain Ω_E and different types of sub-domains, like triangular and rectangular elements for 2D

problems. The formal accuracy of the scheme, in space, is given by the order p of the polynomial expansion of the basis functions Φ. Therefore it is relatively easy to increase locally the accuracy, by using higher order polynomial functions, only where it is needed. On the other hand it also possible and easy to refine the computational sub-domains, like in the Finite Volume methods. After expanding the solution in terms of the set of basis functions, the local approximate solution is then given by

$$U_E(\mathbf{x},t) \approx U_h(\mathbf{x},t) = \sum_{a=1}^{n(p)} U_a(t)\,\phi^a(\mathbf{x}) \text{ in } \Omega_E$$

and the global solution is given by

$$U(\mathbf{x},t) = \sum_{E=1}^{N} U_E(\mathbf{x},t) \text{ in } \Omega.$$

The coefficients U_a are the new unknowns which are recovered by a integral projection into the space of test functions Φ

$$\int_{\Omega_E} \Phi(\mathbf{x})\,U_h(\mathbf{x})\,d\Omega = U_b \int_{\Omega_E} \phi_a(\mathbf{x})\,\phi^b(\mathbf{x})\,d\Omega = \mathbf{ME}_a^b U_b\ .$$

$\mathbf{ME}$ is called the Mass-matrix. Since we use discontinuous test functions the Mass-matrix $\mathbf{ME}$ is block-diagonal with dimension equal to the dimension $n(p)$ of the used local finite element space Φ. Therefore, $\mathbf{ME}$ can be inverted locally

$$U_a = \mathbf{ME}_a^{b\,-1} \int_{\Omega_E} \Phi(\mathbf{x})\,U_h(\mathbf{x})\,d\Omega \tag{2.3}$$

for each computational sub-domain Ω_E. The properties of $\mathbf{ME}$, depending on the finite element space Φ, are analysed in section 2.3. Now the system of equations (2.1) is projected into discontinuous finite element space

$$\int_{\Omega} \Phi(\mathbf{x}) \left(\partial_t \mathbf{U}_h + \partial_k \mathbf{F}^k(\mathbf{U})\right) d\Omega = \int_{\Omega} \Phi(\mathbf{x}) \mathbf{S}(\mathbf{U}_h)\,d\Omega\ ,$$

partial integration and after some arrangement results

$$\partial_t \mathbf{U} \int_{\Omega} \Phi\Phi^t d\Omega + \oint_{\partial\Omega} \Phi \mathbf{F}^k(\mathbf{U})\,d\Gamma_k = \int_{\Omega} \Phi \mathbf{S}(\mathbf{U}_h)\,d\Omega + \int_{\Omega} \mathbf{F}^k(\mathbf{U}_h)\,\partial_k \Phi d\Omega\ .$$

Due to the property (2.2),

$$\mathbf{ME}\partial_t \mathbf{U} + \oint_{\partial\Omega_E} \Phi \mathbf{F}^k(\mathbf{U})\,d\Gamma_k = \int_{\Omega_E} \Phi \mathbf{S}(\mathbf{U})\,d\Omega + \int_{\Omega_E} \mathbf{F}^k(\mathbf{U})\,\partial_k \Phi d\Omega\ . \tag{2.4}$$

Since local discontinuous basis functions are used, there is no coupling at this stage between the neighbouring computational sub-domains Ω_e and the surface

integral in (2.4) is not uniquely defined. The coupling between neighbouring sub-domains is enforced, like in finite volume methods, by replacing the physical flux $\mathbf{F}(\mathbf{U})$ by a constructed numerical flux $\mathbf{F}^k_{num}(\mathbf{U}) = \mathbf{F}^k_{num}(\mathbf{U}_{h,in}, \mathbf{U}_{h,ex})$ defined at the connecting surface $\partial\Omega_{A,B}$. To ensure local conservation of the method, the following property of the numerical flux is required:

$$F_{num,A}(U_{h,A}, U_{h,B}) + F_{num,B}(U_{h,B}, U_{h,A}) = 0 \text{ at } \mathbf{x} : \Omega_A \cap \Omega_B = \partial\Omega_{A,B}$$

and different conservative flux construction schemes, known from finite volume methods, can be used. The numerical fluxes used by the code are reviewed in section 2.5. Since only the states of the physical quantities $\mathbf{U}_{h,int}(\mathbf{x})$, $\mathbf{U}_{h,ext}(\mathbf{x})$ at the interface boundary $\mathbf{x} \in \partial\Omega_{A,B}$ of neighboured sub-domains Ω_A, Ω_B are needed for the construction of the numerical flux, the region of dependence is not affected by the used order p of polynomial approximation. This property makes the DG method efficient for higher order parallel computation and time implicit schemes.

At the computational boundaries $\partial\Omega$ the external values $\mathbf{U}_{h,ext}$ are replaced by the appropriate boundary conditions $\boldsymbol{\gamma}$ projected into the space of discontinuous basis function:

$$\begin{aligned} \oint_{\partial\Omega_E} \Phi \mathbf{F}^k_{num}(\mathbf{U}_{h,int}, \mathbf{U}_{h,ext})\, d\Gamma_k &= \oint_{\partial\Omega_E \neq \partial\Omega} \Phi \mathbf{F}^k_{num}(\mathbf{U}_{h,int}, \mathbf{U}_{h,ext})\, d\Gamma_k \\ &+ \oint_{\partial\Omega_E = \partial\Omega} \Phi \mathbf{F}^k_{num}(\mathbf{U}_{h,int}, \gamma)\, d\Gamma_k \ . \end{aligned} \tag{2.5}$$

Thus after applying the DG method on the conservation law (2.1), the resulting spatial discretisation is given by

$$\begin{aligned} \mathbf{M}^{\mathbf{E}} \partial_t \mathbf{U}_{h,int} &= \int_{\Omega_E} \Phi \mathbf{S}(\mathbf{U}_{h,int})\, d\Omega + \int_{\Omega_E} \mathbf{F}^k(\mathbf{U}_{h,int})\, \partial_k \Phi d\Omega \\ &- \oint_{\partial\Omega_E} \Phi \mathbf{F}^k_{num}(\mathbf{U}_{h,int}, \mathbf{U}_{h,ext})\, d\Gamma_k \\ &- \oint_{\partial\Omega} \Phi \mathbf{F}^k_{num}(\mathbf{U}_{h,int}, \boldsymbol{\gamma})\, d\Gamma_k \ . \end{aligned} \tag{2.6}$$

2.2 Time discretisation

The system of conservation laws (2.1), after using the DGM Ansatz (2.4), is now a system of ordinary differential equations

$$\frac{d\mathbf{U}_h}{dt} = \mathbf{L}_h(\mathbf{U}_h, \boldsymbol{\gamma}) \tag{2.7}$$

with

$$\mathbf{L}_h = \mathbf{M}^{\mathbf{E}-1} \left[\int_{\Omega_E} \Phi \mathbf{S}(\mathbf{U}_h)\, d\Omega + \int_{\Omega_E} \mathbf{F}^k(\mathbf{U}_h)\, \partial_k \Phi d\Omega - \oint_{\partial\Omega_E} \Phi \mathbf{F}^k_{num}(\mathbf{U})\, d\Gamma_k \right] ,$$

which can be integrated in time by several methods. The code uses the explicite TVD multi-step Runge-Kutta (RK) time discretisation method, developed by Shu and Osher [53, 54] which was adapted to the DG Method by Cockburn and Shu [13]. It makes sense to use the equal order $K = p + 1$ of accuracy in time if finite elements $\Phi(P^p)$ with spatial accuracy $p+1$ are used. For each time interval $\Delta t^n = t^{n+1} - t^n$ the values $\mathbf{U}_h^n$ are updated by:

1. set $\mathbf{U}_h^{(0)} = \mathbf{U}_h^n$;
2. for $i = 1, \ldots, K$ compute the intermediate value

$$\mathbf{U}_h^{(i)} = \left[\sum_{k=0}^{i-1} \alpha_{ik} \mathbf{U}_h^{(k)} + \beta_{ik} \Delta t^n \mathbf{L}_h \left(\mathbf{U}_h^{(k)}, \gamma_h \left(t^n + d_k \Delta t^{n+1} \right) \right) \right] \ ; \qquad (2.8)$$

3. set $\mathbf{U}_h^{n+1} = \mathbf{U}_h^{(K)}$.

The parameters for the second and third order RK algorithm are listed below in Table 2.1. A Fourier stability and convergence analysis of the discrete hyperbolic equations gives an upper limit of the time step Δt^n depending on the size Δs of the sub-domain Ω_E and on the highest wave speeds λ_E, given by the maximum eigenvalue of the Jacobian of the fluxes $A = \frac{\partial F}{\partial U}$, explicitly shown in Appendix A. The upper limit of Δt is then given by the well known Courant number $CFL\,(p)$ for explicite time marching schemes:

$$CFL\,(p) \geq \lambda \frac{\Delta t}{\Delta s} \ ,$$

like in other explicite methods. A stability analysis of the DG method by Atkins and Shu [3] shows that there is also a restriction for the time step Δt depending on the order p of the finite element space Φ. By increasing the order p of polynomial expansion the Courant number $CFL\,(p)$ has to decrease

$$CFL\,(p2) < CFL\,(p1) \ \text{ for } p2 > p1.$$

The Courant number $CFL\,(p, K)$ as a function of the order of finite element space p and the order of accuracy in time K, for the one-dimensional linear scalar advection problem

$$\partial_t U + \lambda \partial_x U = 0$$

is listed in Table 2.2. By comparing the DG method with finite difference and volume methods of equal order of accuracy and comparable number of variables this disadvantageous property of the DG method disappears by using less finer grids to get the same accuracy.

order	α_{ik}	β_{ik}	d_k
2	1 $\frac{1}{2}$ $\frac{1}{2}$	1 0 $\frac{1}{2}$	0 1
3	1 $\frac{3}{4}$ $\frac{1}{4}$ $\frac{1}{3}$ 0 $\frac{2}{3}$	1 0 $\frac{1}{4}$ 0 0 $\frac{2}{3}$	0 1 $\frac{1}{2}$

Table 2.1: Parameters for the second and third order Runge-Kutta algorithm.

p	K		
	1	2	3
0	1.0	1.0	1.256
1	0.001	0.333	0.409
2	-	0.06	0.209
3	-	0.02	0.13
4	-	0.01	0.089

Table 2.2: Maximum Courant number $CFL\,(p, K)$ depending on the order of the finite element space p (order $p+1$) and the used Runge-Kutta stage K. Values from Atkins and Shu [3] for the scalar advection problem (- denotes unstable method).

2.3 The basis function for rectangular elements

The characteristic properties of the method are not affected by the choice of the basis and degrees of freedom, since they are determined by the discontinuous element space, the construction of the numerical fluxes and the scheme of time discretisation. In each sub-domain Ω_E a basis of local coordinates $\xi \in [-1,1]$ and $\eta \in [-1,1]$ is defined with the transformation properties regarding to the physical coordinates x_1, x_2

$$\mathbf{x} - \mathbf{x}_0 = \mathbf{J} \begin{pmatrix} \xi \\ \eta \end{pmatrix}$$

with

$$\mathbf{J} \equiv \frac{\partial (x_1, x_2)}{\partial (\xi, \eta)}.$$

The basis functions are polynomials $(1, \xi, \eta, \xi\eta, \xi^2, \eta^2, \ldots)$ of the local coordinates. Since it is time consuming to invert the local mass matrix $\mathbf{ME}$ of a non-orthogonal basis, especially in the case of higher order p approximations, a local orthogonal basis is demanded. The resulting mass matrix $\mathbf{ME}$ is in this case diagonal and easy to invert by hand and therefore less computational operations are needed

$$\mathbf{ME} = \int_{\Omega_E} \Phi \Phi^T d\Omega \equiv \Delta_E \operatorname{diag}(\ldots).$$

The resulting orthogonal basis is then given by

$$\Phi = \left(1, \xi, \eta, \xi\eta, \xi^2 - \frac{1}{3}, \eta^2 - \frac{1}{3}, \cdots\right),$$

where the finite element basis $\Phi(\phi_0, .., \phi_{n(p)})$ for the piecewise constant approximation P^0 is $\Phi = (1)$, for the piecewise linear approximation P^1: $\Phi = (1, \xi, \eta)$ and for the piecewise parabolic approximation P^2 the basis is given by $\Phi = \left(1, \xi, \eta, \xi\eta, \xi^2 - \frac{1}{3}, \eta^2 - \frac{1}{3}\right)$, with the corresponding degrees of freedom

$$U_a(t) = \left(\bar{U}(t), U_\xi(t), U_\eta(t), U_{\xi\eta}(t), U_{\xi\xi}(t), U_{\eta\eta}(t), \ldots\right)$$

evolved in time. In section 2.4 it is also shown that a local orthogonal basis requires less computational effort for use of slope limiting, which is needed for higher order $p \geq 1$ finite elements. In the case of an orthogonal basis, the mean values $\bar{U}$ in Ω_E of the approximated solution U_h are nothing but the coefficient of the $P^0 : U_h^0$ part of U_h, since:

$$\bar{U}_E = \frac{1}{\Delta\Omega_E} \int_{\Omega_E} U_h d\Omega = \frac{1}{\Delta\Omega_E} \int_{\Omega_E} \sum_{a=1}^{n(p)} U_a \phi^a d\Omega = U_1 = U_h^0 \text{ in } \Omega_E.$$

2.3.1 Mass Matrix for the P^1 and P^2 basis

For the polynomial expansion of order P^1 in two dimensions the approximate solution is given by

$$U_h(\mathbf{x},t) = U_0(t) + U_\xi(t)\,\phi_1(\xi) + U_\eta(t)\,\psi_1(\eta) \tag{2.9}$$

with the property

$$\int_{\Omega_E} U_h(\mathbf{x},t)\,d\Omega = U_0(t)\,\Delta\Omega_E$$

where U_0 is the mean value $\bar{U}$ of U_h in the sub-domain Ω_E. The basis is orthogonal, and therefore the mass matrix

$$\mathbf{ME}(P^1) = \int_{\Omega_E} \Phi\Phi^T d\Omega = \Delta\Omega_E \,\mathrm{diag}\left(1, \frac{1}{3}, \frac{1}{3}\right) \tag{2.10}$$

is diagonal. For the P^2 expansion

$$U_h(\mathbf{x},t) = \sum_{i=1}^{3} U_i(t)\,\phi^i(\xi,\eta) \tag{2.11}$$

the resulting mass matrix is given by

$$\mathbf{ME}(P^2) == \Delta\Omega_E \,\mathrm{diag}\left(1, \frac{1}{3}, \frac{1}{3}, \frac{1}{9}, \frac{4}{45}, \frac{4}{45}\right). \tag{2.12}$$

.

2.4 The slope limiter

For elements of order $p = 0$, the piecewise constant element space, the numerical viscosity is large enough, due to the constructed numerical fluxes, to ensure stability of the scheme, but with the disadvantage of a large smoothing of discontinuities. In the case of higher order $p \geq 1$ elements the numerical viscosity is too small to ensure stability of the method. At discontinuities spurious oscillations are arising in the solution and are not damped out. To get a stable high order DG method, Cockburn and Shu [13] introduce a local conservative slope limiting to the DG Method and preserve a total variation bound in the means (TVBM) of the conservative variables. Here the slope limiter is applied onto a scalar hyperbolic equation.

- The following properties of the slope limiting operator $\boldsymbol{\Lambda\Pi}$ are required:

  1. In the case of small variation of the approximate solution u_h the order of accuracy should not be affected

$$\boldsymbol{\Lambda\Pi} U_h = U_h \ . \tag{2.13}$$

2. Local conservation of the conservative variable U_h

$$\int_{\Omega_E} \mathbf{\Lambda\Pi} U_h d\Omega = \int_{\Omega_E} U_h d\Omega = \bar{U} \tag{2.14}$$

3. The gradient of $\mathbf{\Lambda\Pi} U_h$ is not larger than that of U_h

$$\partial_{(\xi,\eta)} \mathbf{\Lambda\Pi} U_h \leq \partial_{(\xi,\eta)} U_h \tag{2.15}$$

The assumption is made that spurious oscillations are present in U_h only if they are also present in the piecewise linear part P^1 of $U_h : U_h^1 = \sum_{a=1}^{n(p=1)} U_a \phi^a$. In the case that no oscillations are present in U_h^1:

$$\mathbf{\Lambda\Pi} U_h^1 = U_h^1$$

then it is assumed that there are no nonlinear oscillations in $U_h \in P^p$ and therefore no limiting, formally $\mathbf{\Lambda\Pi} = 1$:

$$\mathbf{\Lambda\Pi} U_h = U_h \ .$$

If

$$\mathbf{\Lambda\Pi} U_h^1 \neq U_h^1 \ ,$$

then there are oscillations in U_h^1, and therefore in U_h and all degrees of freedom $U_a \in U_h^{\geq 2}$ are set to zero.

$$U_{a\,(p\geq 2)} = 0$$

and limiting the remaining P^1 part U_h^1:

$$\mathbf{\Lambda\Pi} U_h = \mathbf{\Lambda\Pi} U_h^1 \ .$$

The slope limiting operator $\mathbf{\Lambda\Pi}$ is applied to the K stage Runge-Kutta method by:

1. set $\mathbf{U}_h^{(0)} = \mathbf{U}_h^n$;

2. for $i = 1, \ldots, K$ compute and limit the intermediate value

$$\mathbf{U}_h^{(i)} = \mathbf{\Lambda\Pi} \left[\sum_{k=0}^{i-1} \alpha_{ik} \mathbf{U}_h^{(k)} + \beta_{ik} \Delta t^n \mathbf{L}_h \left(\mathbf{U}_h^{(k)}, \gamma_h \left(t^n + d_k \Delta t^{n+1} \right) \right) \right] \ ; \tag{2.16}$$

3. set $\mathbf{U}_h^{n+1} = \mathbf{U}_h^{(K)}$.

2.4.1 Slope limiting operator $\Lambda\Pi$ for rectangular sub-domains

In the case of rectangular sub-domains with the properties $dx_1 = \frac{\partial x_1}{\partial \xi} d\xi$, $dx_2 = \frac{\partial x_2}{\partial \eta} d\eta$ the properties 2.13, 2.14 and 2.15 of the limiter are achieved by the following construction:
The limiting is only applied on the piecewise linear degrees of freedom in the sub-domain $\Omega_{I,J}$

$$\begin{pmatrix} U_\xi \\ U_\eta \end{pmatrix} = \mathbf{J} \begin{pmatrix} \partial_{x_1} \\ \partial_{x_2} \end{pmatrix} U \text{ in } \Omega_{I,J} \tag{2.17}$$

The inner sub-domain gradient of the P^1 part of U_h in direction x_1 is

$$\Delta_E = \partial_\xi U_h^1 = U_\xi \text{ in } \Omega_{I,J} \tag{2.18}$$

and the outer gradients of the mean values $\bar{U}$ of neighbouring left $\Omega_{I-1,J}$ and right Ω_{I+1_J} sub-domains are defined by

$$\Delta_+ = \bar{U}_{I+1,J} - \bar{U}_{I,J} = \frac{1}{\Delta\Omega_{I+1,J}} \int_{\Omega_{I+1,J}} U_h d\Omega - \frac{1}{\Delta\Omega_{I,J}} \int_{\Omega_{I,J}} U_h d\Omega, \tag{2.19}$$

$$\Delta_- = \bar{U}_{I,J} - \bar{U}_{I-1,J} = \frac{1}{\Delta\Omega_{I,J}} \int_{\Omega_{I,J}} U_h d\Omega - \frac{1}{\Delta\Omega_{I-1,J}} \int_{\Omega_{I-1,J}} U_h d\Omega. \tag{2.20}$$

The function $\bar{m}$ is the TVB corrected minmod function defined by

$$\bar{m}\left(\Delta_E, \Delta_+, \Delta_-\right) = \begin{cases} \Delta_E \text{ , if } |\Delta_E| \leq M\Delta x_1^2 \\ m\left(\Delta_E, \Delta_+, \Delta_-\right) \text{ otherwise} \end{cases} \tag{2.21}$$

where M the TVB parameter and the minmod function is defined by

$$m\left(\Delta_E, \Delta_+, \Delta_-\right) = \begin{cases} s \ \min|\Delta_i| \text{ , if } s = \text{sign}\Delta_E = \text{sign}\Delta_+ = \text{sign}\Delta_- \\ 0 \text{ otherwise.} \end{cases} \tag{2.22}$$

The new coefficients are achieved by integral projection into the P^1 finite element space Φ_1

$$\int_{\Omega_{I,J}} \Phi_1 \ \bar{m} \ d\Omega \tag{2.23}$$

and, since the P^1 part of U_h is orthogonal the second requirement for conservation, (2.14) is realised. The first requirement (2.13), not to change the order of the method near smooth extrema where the values of u_ξ or u_η is of order $O\left(\Delta\xi^2\right)$, is satisfied by the TVB parameter $M > 0$. The method is not sensitive in a large range of M, but by setting M too small the method is reduced independent of the expansion p mostly to second order accuracy. An estimate of the TVB parameter can be done by a Fourier analysis, showing that the local variations should be in a linear regime. By taking too large values of M and the variations of U_h are in

the nonlinear range, spurious oscillations can occur. Like Cockburn and Shu [13] the code use a TVB parameter $M = 50$.

Working with an orthogonal basis, less computational effort is needed, since in this case the mean values $\bar{U}$ are given by the P^0 part of the expansion of U_h, i.e., the expansion coefficient U_0

$$\Delta_+ = \bar{U}_{I+1,J} - \bar{U}_{I,J} = U_{0\,I+1,J} - U_{0\,I,J}, \tag{2.24}$$

$$\Delta_- = \bar{U}_{I,J} - \bar{U}_{I-1,J} = U_{0\,I,J} - U_{0\,I-1,J}. \tag{2.25}$$

2.4.2 Slope limiting for systems of equations

For systems of nonlinear equations, like 2.1, it is possible to apply the slope limiter $\mathbf{\Lambda\Pi}$ directly to each component of the vector of the conservative variables $\mathbf{U}_h$, like in the case of a scalar equation. But a better resolving of discontinuities is achieved by limiting the vector of the corresponding characteristic variables $\mathbf{C}(\mathbf{U}_h)$ of the conserved ones:

$$\begin{aligned} \mathbf{\Delta}_E &= \mathbf{R}^{-1}\mathbf{U}_\xi && \text{in } \Omega_{I,J} \\ \mathbf{\Delta}_+ &= \mathbf{R}^{-1}\left(\bar{\mathbf{U}}_{I+1,J} - \bar{\mathbf{U}}_{I,J}\right) \\ \mathbf{\Delta}_- &= \mathbf{R}^{-1}\left(\bar{\mathbf{U}}_{I,J} - \bar{\mathbf{U}}_{I-1,J}\right) \end{aligned} \tag{2.26}$$

and then apply the scalar limiter to each component $\mathbf{\Delta}$ and transform the solution back to the system of conservative variables, by

$$\mathbf{\Lambda\Pi}\,\mathbf{U}_h = \mathbf{R}\bar{\mathbf{m}}.$$

$\mathbf{R}$ and $\mathbf{R}^{-1}$ are the matrices of the right and left eigenvectors, which diagonalise the Jacobian of the flux:

$$\mathbf{R}^{-1}\frac{\partial \mathbf{F}\left(\bar{\mathbf{U}}_{I,J}\right)}{\partial \bar{\mathbf{U}}}\mathbf{R} = \mathbf{\Lambda}\ ,$$

specified in appendix A. A comparison between the slope limiting applied on the conserved and the limiting of the characteristic variables is shown in figure 2.1 for a one-dimensional Riemann problem. By limiting the conservative variables spurious oscillations are visible and the contact discontinuity is less resolved than in the case of limiting the characteristic variables.

2.5 The numerical fluxes

The numerical fluxes $F_{num} = F_{num}(U_h(x_{int} \in \partial\Omega), U_h(x_{ext} \in \partial\Omega))$ are computed from the physical states at the interfaces of connecting sub-domains. To enforce

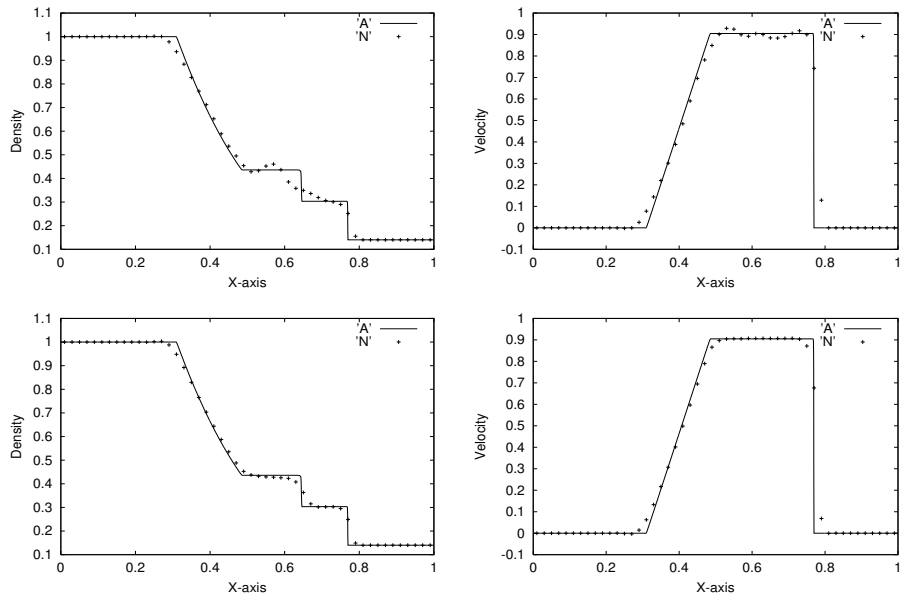

Figure 2.1: Results of a low resolution 1D Riemann shock tube problem at time $t = 0.16$. The upper panel shows the density d and velocity v for slope limiting of the conservative variables $\mathbf{U}$. The lower panel shows the results for slope limiting of the characteristic variables $\mathbf{C}$. The analytical solution is shown by the solid line, (+) numerical with a grid resolution of 50 elements in the computational domain..

local conservation of the scheme, the following property

$$F_{num,a}(U_{h,a}(x_{int}), U_{h,a}(x_{ext}) + F_{num,b}(U_{h,b}(x_{int}), U_{h,b}(x_{ext}) = 0, \tag{2.27}$$

at $\partial\Omega_{ab} \in \Omega_a \cap \Omega_b$ has to be required for the construction of the numerical fluxes.

2.5.1 The Lax-Friedrich flux

The Lax-Friedrich flux is simple to construct, needs less computational effort and enforces the entropy conditions at shocks and rarefaction waves, but for the prize of introducing a higher intrinsic numerical viscosity into the scheme than other flux reconstruction methods. Since only an estimate of the biggest eigenvalue of the flux Jacobian is needed, the Lax-Friedrich flux is useful for systems of equations, where the eigenvalues are not known, of complicated structure or computationally expensive to recover

$$F_{num}(U_{int}, U_{ext}) = \frac{1}{2}\left[F^k\left(U_{int}\right) n_k + F^k\left(U_{ext}\right) n_k - \alpha\left(U_{ext} - U_{int}\right)\right] \ . \tag{2.28}$$

n_k is the outward directed unit vector of the sub-domains surface. The conserved variables U_{int}, U_{ext} are evaluated at the interface of neighbouring sub-domains

and the numerical viscosity parameter Λ is an estimate of the largest eigenvalue, in absolute values, of the mean values $\bar{U}_{int}$, $\bar{U}_{ext}$ in the connecting sub-domains

$$\alpha = \max\left(|\lambda(\bar{U}_{int})|, |\lambda(\bar{U}_{ext})|\right) .$$

2.5.2 The Marquina flux

This concept of flux vector splitting, introduced by Marquina [17], is less numerically viscous than the Lax-Friedrich flux, but needs the knowledge of the characteristic system of the conservation laws

$$\phi_l = R^{-1}_{lm} F_m \ , \quad \omega_l = R^{-1}_{lm} U_m . \tag{2.29}$$

The corresponding eigenvalues λ_l are defined that for $\lambda_l > 0$ the l characteristic waves are outward directed at the connecting surface $\partial\,\Omega = \Omega_{int} \cap \Omega_{ext}$. Then for each different wave l, of both sides of the connecting domains, it is analysed if there is an inflow, outflow, shock or a rarefaction wave. The outward directed wave de-composite ϕ^+_l is therefore

$$\phi^+_l = \begin{cases} 0 & \text{if } \lambda^{int}_l < 0 \text{ and } \lambda^{ext}_l < 0 \\ \phi^{int}_l & \text{if } \lambda^{int}_l > 0 \text{ and } \lambda^{ext}_l > 0 \\ \frac{1}{2}\left(\phi^{int}_l + \alpha_l \omega^{int}_l\right) & \text{if } \lambda^{int}_l \lambda^{ext}_l < 0, \end{cases} \tag{2.30}$$

with $\alpha_l = \max\left(|\lambda^{int}_l|, |\lambda^{ext}_l|\right)$ and the inward directed part ϕ^-_l of the flux is given by

$$\phi^-_l = \begin{cases} 0 & \text{if } \lambda^{int}_l > 0 \text{ and } \lambda^{ext}_l > 0 \\ \phi^{ext}_l & \text{if } \lambda^{int}_l < 0 \text{ and } \lambda^{ext}_l < 0 \\ \frac{1}{2}\left(\phi^{ext}_l - \alpha_l \omega^{ext}_l\right) & \text{if } \lambda^{int}_l \lambda^{ext}_l < 0. \end{cases} \tag{2.31}$$

The superscript ^{int} stands for the computational domain Ω_{int} surrounded by the surface $\partial\Omega$ and the superscript ^{ext} stands for the neighbouring domains Ω_{ext}. The Marquina flux for the conserved variables is then given by

$$F^{num}_l = \left(R^{int}_{lm}\phi^+_m + R^{ext}_{lm}\phi^-_m\right) . \tag{2.32}$$

In the case of $\lambda^{int}_l \lambda^{ext}_l > 0$ the Marquina flux reduces to the Steger-Warming [55] splitting, up-winding of the l-wave characteristic variables. At shocks and rarefaction waves, the internal and external eigenvalues have different signs and the Marquina scheme reduces to the Lax-Friedrich method in the system of characteristic variables. Since for each surface integral the fluxes have to be transformed into the system of characteristic variables and a controlling by IF-clauses has to be made, the Marquina flux scheme needs more computational time than the Lax-Friedrich recipe.

2.6 Numerical quadrature of surface and volume integrals

The numerical integration is done by the method of Gauss. The analysis in [11] shows that for a polynomial basis P^p of order p the numerical quadrature of surface integrals must be exact of order $2p+1$ and the quadrature rules for the volume integral of order $2p$. This comes from fact that the hydrodynamical fluxes and sources are nonlinear functions of the conservative variables $\mathbf{U}_h$. Depending on the used order p, the Gauss rules for the surfaces are

$$\oint_{-1}^{1} f(s)ds \approx \sum_{i=1}^{n(p)} \omega_i f(p_i) \tag{2.33}$$

and for the volume integral a tensor product is used

$$\int_{\Omega} f(x,y)\, d\Omega \approx \sum_{i=1}^{n(p)} \sum_{j=1}^{n(p)} \omega_i \omega_j f(\zeta_i, \zeta_j) \ , \tag{2.34}$$

where ζ_i are the Gauss points with corresponding weights ω_i. The numerical quadrature becomes more computational time consuming by increasing order p of polynomial expansion and most of CPU-time is needed to calculate the element integrals. In the case of relativistic hydrodynamics a further increase of computational effort occurs, since at each Gauss point ζ_i a nonlinear algebraic equation has to be solved to recover the primitive variables from the conserved ones, by using a one dimensional Newton-Raphson routine, discussed in the following section 2.7. To circumvent the numerical quadrature, a quadrature-free approach was developed by Atkins and Shu [3, 12] for the nonrelativistic Euler equations. By applying this approach to nonlinear conservation laws a specially handling of the conserved variables, the corresponding fluxes and sources becomes absolutely essential. If this approach is also applicable on the relativistic equations has to be analysed.

p	Gauss points ζ_i	Weights ω_i
1	$-1/\sqrt{3}$, $1/\sqrt{3}$	1, 1
2	$-\sqrt{3/5}$, 0, $\sqrt{3/5}$	5/9, 8/9, 5/9

Table 2.3: Parameters for the Gauss quadrature.

2.7 Recovering the primitive variables

To compute the fluxes, sources and for applying the slope limiter on the characteristic variables, the primitive variables $w = (\rho, v_i, p)$ of the system have to be computed. The recovering of the primitive variables from the conserved ones is easy for ideal Newtonian hydrodynamics, but in the case of ideal relativistic hydrodynamics the recovering procedure can not be formulated in closed form. Therefore, a one-dimensional Newton-Raphson method, introduced by Martí, Ibáñez and Miralles [37], is used for the recovering of the primitive variables, by finding the root of:

$$f(p) = (\gamma - 1)\rho\epsilon - p \tag{2.35}$$

The explicit algorithm is explained in appendix B. A further way to recover the primitives was introduced by Duncan and Hughes [18]. They solved iteratively the quartic equation

$$\left[\gamma v \left(E - Mv\right) - M\left(1 - v^2\right)\right]^2 - \left(1 - v^2\right) v^2 \left(\gamma - 1\right)^2 D^2 = 0, \tag{2.36}$$

where $M = \sqrt{M_i M^i}$ is the momentum and D, M_i, E are the conservative variables of the fluid measured in the lab frame.

In regions, where the states of the flow vary smoothly, the Newton-Raphson routine requires one to 4 iterations to reach a relative accuracy of 10^{-10}. At discontinuities the required iterations are in the range of 10. Simulating highly relativistic flows with Lorentz factor $W > 10$ in 2D it happens some times, if discontinuities are involved, that the requested accuracy could not be reached. In this case the calculation is repeated at time t^n and the time step is decreased by a factor of two.

Chapter 3

Code testing

The Newtonian test problems are computed with the relativistic version of the code, to check if the code can handle low velocity $v \ll 1$ and low specific internal energy $\epsilon \ll \rho$ well. One-dimensional test problems are solved by the two dimensional version of the code. For integration in time the two-step Runge-Kutta method was used and the CFL number was set in all computations to CFL=0.3, except if the recovering of the primitive variables was not possible, which some times occurs in two-dimensional highly relativistic simulations at discontinuities. The space was discretised by rectangular sub-domains and a P^1 basis was used, therefore the method is second order in space, except at discontinuities. The Lax-Friedrich method 2.28 was used to compute the fluxes, which is slightly more diffusive at contact discontinuities than the computationally more expensive Marquina flux.

3.1 The Woodward and Colella test problems

This section deals with the three test problems investigated in the fundamental article of Woodward and Colella [61]. In their review article an extensive comparison study of various numerical methods for simulating ideal hydrodynamic flows in the Newtonian limit was discussed. Each of these tests inhere different problems to be solved by the code. The two-dimensional test problems are also studied in the article of Cockburn and Shu [13] using the DG method with a P^1 and P^2 polynomial basis and for domains discretised by rectangular and unstructured triangular elements.

3.1.1 Newtonian 1D interacting blast wave problem

This one-dimensional test problem involves multiple interaction of strong shocks and rarefaction with each other and contact discontinuities, caused by initial three different states of pressure in the domain of computation of size $x \in [0 :$

1] with reflecting boundaries. In the hole range initially the rest mass density ρ is set to a constant value 10^5 and the velocity is set to zero. In the range $x \in [0, 0.1]$ the pressure is given by $p = 10^3$, for $x \in]0.1, 0.9[$ $p = 10^{-2}$ and for $x \in [0.9, 1]$ the pressure is set to $p = 10^2$. The gas has a adiabatic index of $\gamma = 1.4$. The space and time units are renormalised to the speed of sound given by $c_{s0} = \sqrt{\gamma p_0/\rho}$ with $p_0 = 1$. Since the rest mass density $\rho \gg p$, the problem is intrinsically nonrelativistic. The resulting distributions of rest mass density at time 0.038, for different resolution in space are shown in Figure 3.1. Compared to the results presented in the article of Woodward and Colella [61] the accuracy of the solution is between that of the MUSCL scheme and that of the Piecewise Parabolic Methods (PPM), but the very good resolution of the contact discontinuity of the PPM codes is not reached.

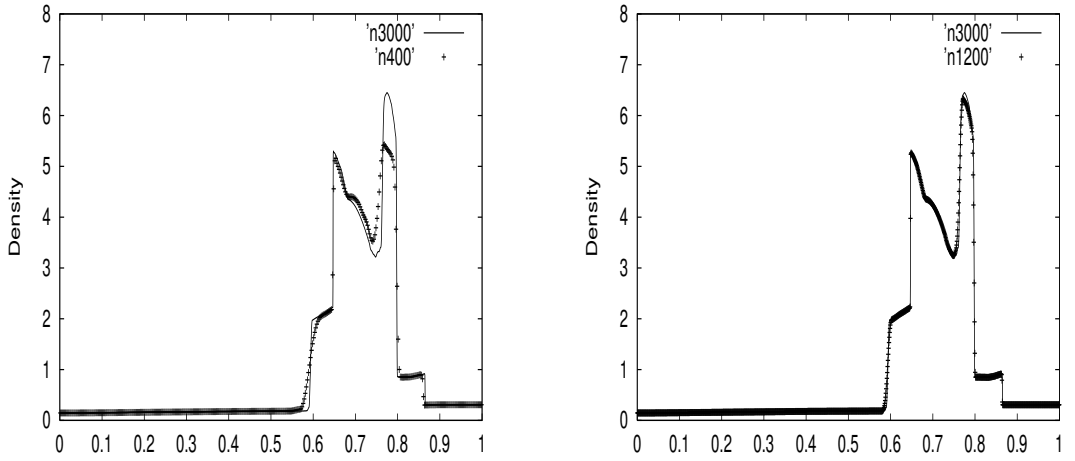

Figure 3.1: The rest mass density $\times 10^5$ of the interacting blast wave problem at time t=0.038. The resolution of the left figure is $\Delta x = 1/400$ and of the right one $\Delta x = 1/1200$. The solid line in both figures was obtained from a computation with a very high resolution of $\Delta x = 1/3000$.

3.1.2 Newtonian 2D double Mach reflection

This test problem was also studied by Woodward and Colella with different numerical methods. Initially a Mach 10 shock in air, $\gamma = 1.4$ is reflected by a wall which makes an 60° angle to the right propagating shock front. The reflecting wall lies in the range $x \in [1/6, 4]$ of the x-axis at $y = 0$. In the region $x - y/\tan 60° < 1/6$ initially the values are set to the post-shock conditions and elsewhere to the states of the pre-shocked air. At the upper boundary, at $y = 1$,

the boundary condition is time dependent to follow the motion of the shock. This is done by setting post shock values for

$$x < x_s(t) = \frac{M c_s}{\cos 30^\circ} t + 1/6 + 1/\tan 60^\circ \ ,$$

where M is the Mach number and c_s is the sound speed of the un-shocked air, and pre-shock values otherwise. To be in the Newtonian limit, $\epsilon \ll \rho$, and all values are renormalised to the values of the Woodward and Colella calculation. At evolution time t=0.2 a complicated flow pattern develops characterised by two reflected Mach shocks with two contact discontinuities. The reflected shock and the inclined shock merge at the leading triple point. At the reflecting wall a jet-like structure with a mushroom-shaped head develops and propagate to the right behind the strong Mach shock. In figure 3.2 the density at time 0.2, with different element resolution, is shown. Compared to the results of Woodward and Colella the accuracy is between that of the MUSCL scheme and that of the PPM method, similar to the interacting blast wave problem. Even in the low resolution run ($\Delta x = 1/30$) all flow patterns are developed and are located at the correct position. Further a calculation with a non-uniform spacing of elements, shown in the figures 3.3 and 3.4, was done, to study how the solution of the reflected and moving shock is influenced by the use of non-uniform grid scaling. Like in the case of uniform grid scaling the flow pattern is correctly developed.

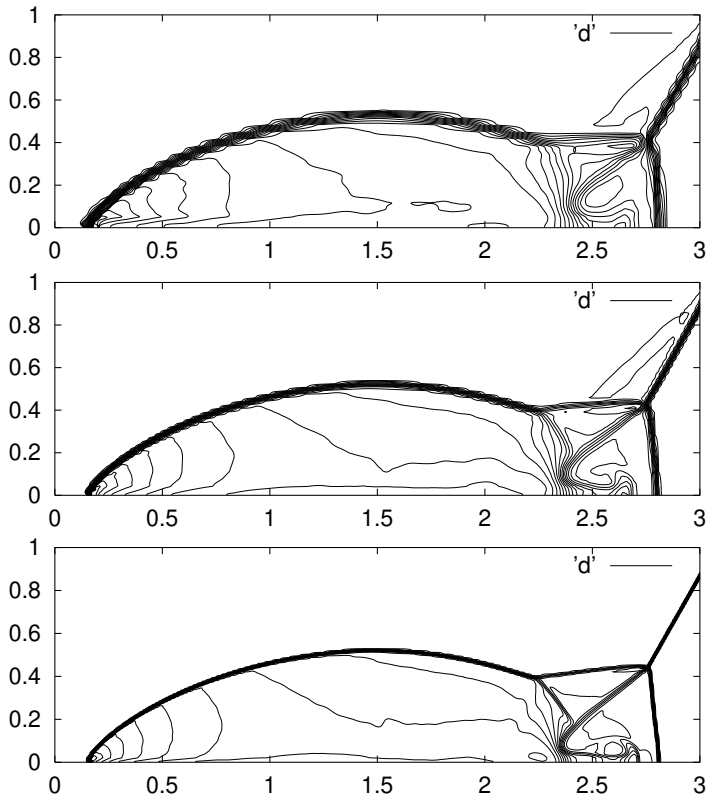

Figure 3.2: The density of a double Mach reflection of a Mach 10 shock wave from a wall is shown at evolution time t=0.2 for a uniform element resolution. Element resolution from top to down: $\Delta x = \Delta y = 1/30, 1/60, 1/120$. 30 equally spaced density contours from the minimum to the maximum values are shown.

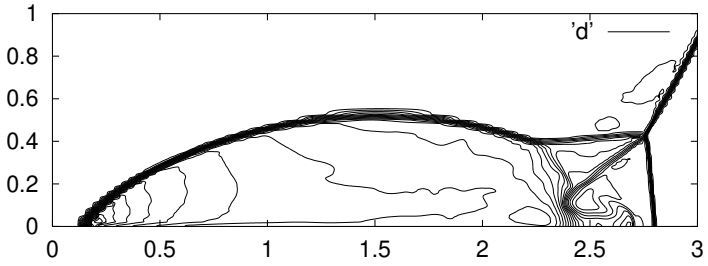

Figure 3.3: The density of the DMR problem for a discontinuous scaling of the grid in both directions. Grid scaling in x direction $\Delta x = 1/30$ for $x \in [0, 1.5[$, $\Delta x = 1/60$ for $x \in [1.5, 2[$ and $\Delta x = 1/30$ for $x \in [0, 3.5]$. Grid scaling in y direction $\Delta y = 1/120$ for $y \in [0, 25]$, $\Delta y = 1/60$ for $y \in]0.25, 0.5]$ and $\Delta y = 1/30$ for $y \in]0.5, 1]$. 30 equally scaled density contours from the minimum to the maximum values are shown.

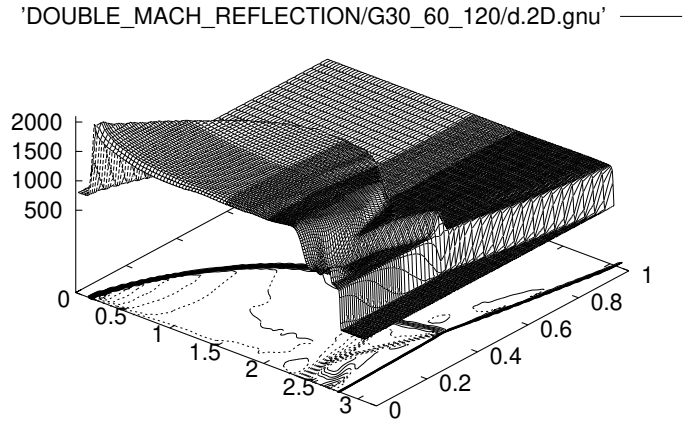

Figure 3.4: Surface plot of the DMR problem for a discontinuous scaling of the grid in both directions, same as in Fig. 3.3. Grid scaling in x direction $\Delta x = 1/30$ for $x \in [0, 1.5[$, $\Delta x = 1/60$ for $x \in [1.5, 2[$ and $\Delta x = 1/30$ for $x \in [0, 3.5]$. Grid scaling in y direction $\Delta y = 1/120$ for $y \in [0, 25]$, $\Delta y = 1/60$ for $y \in]0.25, 0.5]$ and $\Delta y = 1/30$ for $y \in]0.5, 1]$

3.1.3 Newtonian 2D Mach 3 wind tunnel with a step problem

This two-dimensional test problem treats of an initially uniform Mach 3 flow propagating to the right in a wind tunnel containing a step. The wind tunnel is 3 length units long and 1 length unit high. The step begins 0.6 length units from the left inflow boundary and is 0.2 length units high. Outflow boundary conditions are set at the right computational boundary $x = 3$ and for the upper, lower and step boundaries reflecting conditions are applied. The corner of the step is a singularity for the flow, where large numerical errors occur. In contrast to the calculations of Woodward and Colella no special handling at the corner of the step, like the entropy fix, was done. This leads to an erroneous entropy layer and a spurious Mach stem at the bottom wall. Cockburn and Shu [13] show that these numerical artifacts decrease if the mesh is refined at the corner of the step. In figure 3.5 the resulting flow pattern of the density at evolution time 4.0 is shown. By ignoring the numerical artifacts all shocks and discontinuities occur at the correct location. In contrast to the solution of this problem computed by the ZEUS code (Stone and Norman [56]), there is no large dependence of the flow pattern on the grid resolution used in our computations.

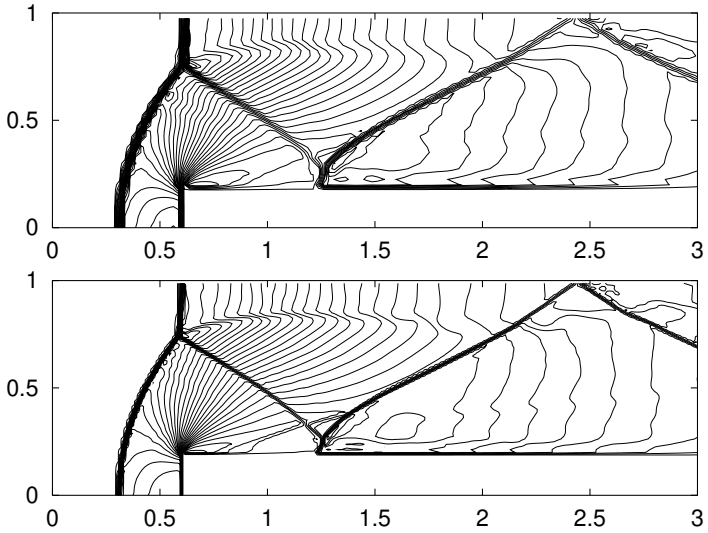

Figure 3.5: The density at time 4.0 of the Mach 3 wind tunnel with a step is shown for a uniform element resolution. Element resolution from top to down $\Delta x = \Delta y = 1/40, 1/80$. 30 equally scaled density contours from the minimum to the maximum values are shown.

3.2 The 1D mildly relativistic Riemann problem

This test problem considers the time evolution of an initially discontinuous state of a fluid at rest $v = 0$. In the range $x \in [0, 0.5]$ the initial values are given by $\rho = 10$, $\epsilon = 2$ and in $x \in]0.5, 1]$ they are given by $\rho = 1$, $\epsilon = 10^{-6}$ with the gas adiabatic $\gamma = 5/3$. The fluid in the high pressure region on the left is relativistic in the thermodynamical point of view, but develops only mildly relativistic dynamical velocities. The formation of an intermediate state is bounded by a shock wave propagating to the right and a transonic rarefaction wave propagating to the left side. The fluid is accelerated by the pressure gradient to the mildly relativistic speed v=0.72c.

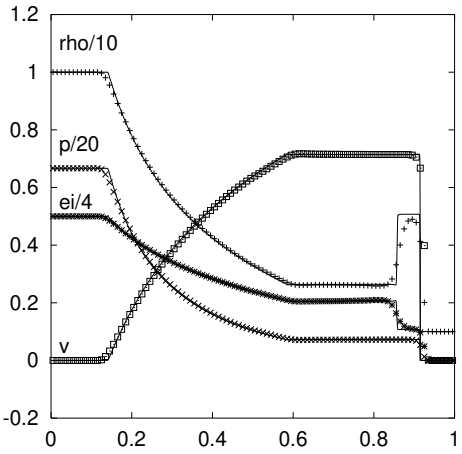

Figure 3.6: Numerical (symbols) and exact (lines) solution of the mildly relativistic Riemann problem. The figure shows the resulting states of the proper rest-mass density rho, pressure p, specific internal energy ei and flow Lorentz factor W at time t=0.5. The grid resolution was set to 100 elements per unit length.

3.3 The 1D relativistic planar shock reflection

In this test problem the code has to handle the reflection of strong shock waves caused by the collision of two cold relativistic gas flows. The initial data are in the range $0 \leq x \leq 1$: $\rho_L = 1$, $\epsilon_L = 2.29\ 10^{-5}$, $v_L = v_f$ and for $1 < x \leq 2$: $\rho_R = 1$, $\epsilon_R = 2.29\ 10^{-5}$, $v_R = -v_f$. In figure 3.7 the physical states, at time 2.0, of the reflecting shock, propagating to the left, is shown for an inflow velocity of $v_i = 0.9c$. Figure 3.8 shows the rest mass density jumps in logarithmic scale for different inflow velocities v_f. The largest possible inflow Lorentz factor was given

by 2.236×10^4; for higher inflow velocities this version of the code was unable to compute the primitive variables from the conserved ones at the discontinuities.

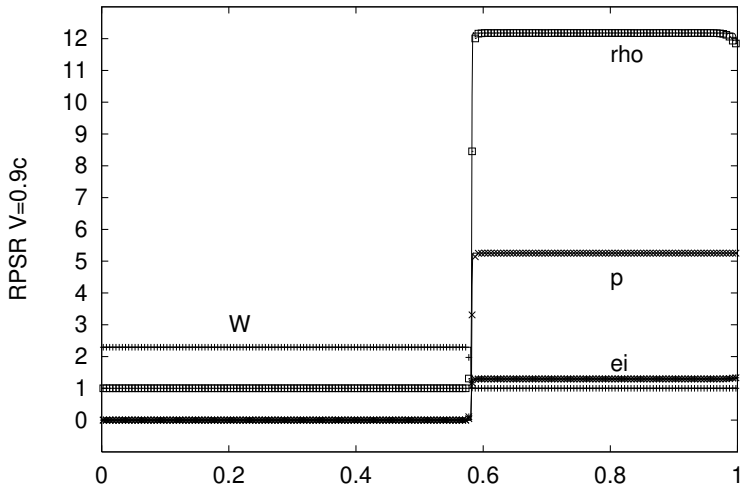

Figure 3.7: Numerical (symbols) and exact (lines) solutions of the mildly relativistic planar shock reflection problem, $v = 0.9c$. The figure shows the the distribution of the proper rest-mass density rho, pressure p, specific internal energy ei and flow Lorentz factor W at time t=2.0. The resolution was set to 200 elements per unit length.

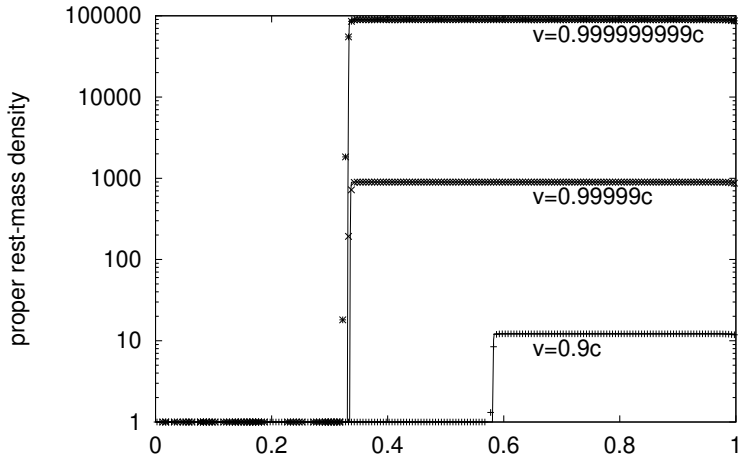

Figure 3.8: Numerical (symbols) and exact (lines) solutions of the relativistic planar shock reflection problem for different inflow velocities. The figure shows the resulting proper rest-mass density as a function of the inflow velocities v at time t=2.0 and 200 elements per unit length. The largest inflow Lorentz factor is $W = 2.236 \times 10^4$

3.4 The 1D relativistic blast wave

The initial states of the intrinsic relativistic blast wave problem are: for $x \leq 0.5$ $\rho_l = 1$, $v_l = 0$, $p_l = 10^3$ and for $x > 0.5$: $\rho_r = 1$, $v_r = 0$, $p_r = 10^{-2}$. On the left side, in the hot high pressure region, the test problem is extremely relativistic in the thermodynamic sense, since the internal specific energy ϵ is much larger than the energy rest-mass density ρ of the fluid. Figure 3.9 shows the physical states of this test at time 0.36 with 400 elements per unit length. A thin zone of high rest mass density is accumulated by the leading shock and becomes thinner and thinner for higher relativistic flow speeds. The decreasing in size of this region occurs, because the contact discontinuity moves with the velocity $v_{c.d.}$ of the pressure accelerated flow and the shock moves with a higher velocity $v_s > v_f$. But since the velocities must be sub-luminal, $v_{c.d.} < v_s < 1$, the size of the swept up gas decreases for higher flow velocity. This kind of problem also occurs in the case of ultra-relativistic jet computations and, therefore, a higher resolution in space is needed than in the Newtonian case, to resolve the contact discontinuity and the shocked ambient medium. A comparison between the Newtonian case and the relativistic one is shown in figure 3.10. To get a Newtonian flow, the value of the rest-mass density was changed to $\rho_{new} = 10^5 \rho_{rel}$, therefore the ratio of the specific internal energy and rest mass energy is in the Newtonian limit and the flow is accelerated only to a non-relativistic velocity of $v = 0.057c$. Now the region of accumulated initial cold gas is much larger than in the relativistic case shown in the right figure of 3.10.

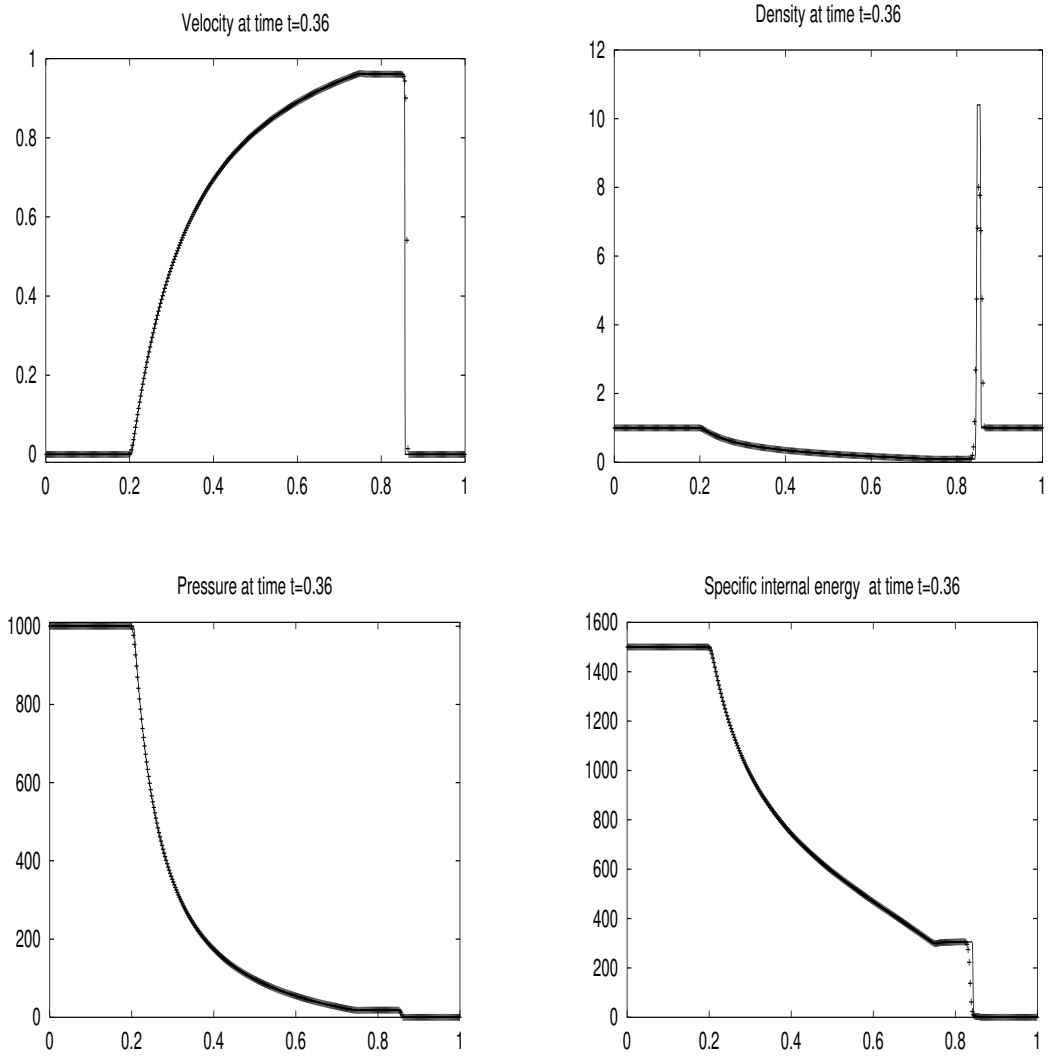

Figure 3.9: Numerical (symbols) and exact (lines) solutions at time 0.36 of the relativistic blast wave problem. Resolution: $\Delta x = 1/400$.

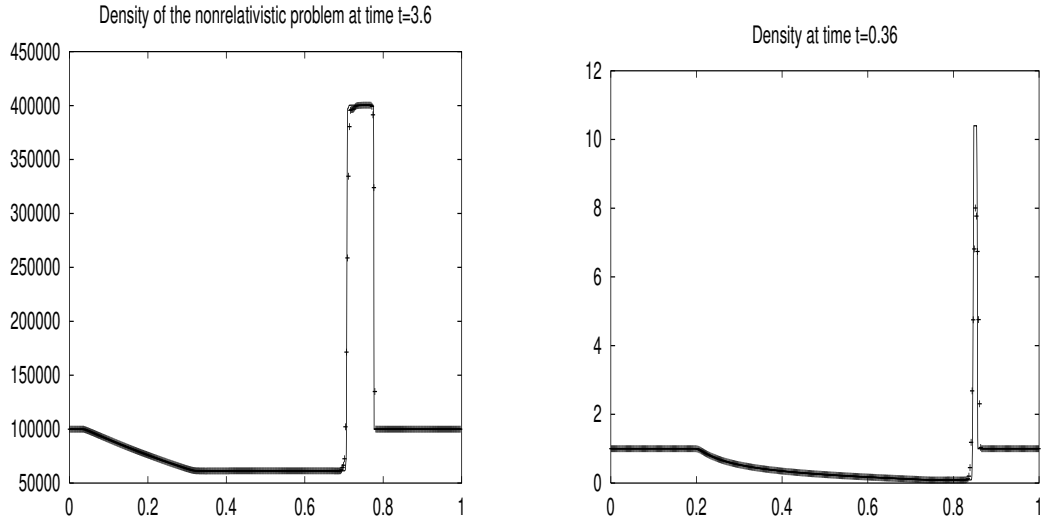

Figure 3.10: A comparison study of the Newtonian and relativistic blast wave problem. Shown is the rest-mass density ρ of the nonrelativistic (left) problem at time 3.6 and the relativistic (right) case at time 0.36. The space resolution is $\Delta x = 1/400$.

Chapter 4

Astrophysical flow problems

4.1 Jet simulations

In this section the code is applied to the astrophysical problem of hydrodynamic jet propagation in homogeneous ambient media. In the first part the dependence of the evolving flow structure on the grid resolution of a Newtonian jet is analysed. In the second part the propagation of relativistic jets with different initial flow parameters are summarised.

4.1.1 Resolution study of a hydrodynamic Newtonian Mach 6 jet

In this section the dependence on the grid resolution of the developing flow structure of a Newtonian axially symmetric jet is investigated. For this problem the conservation laws are solved in cylindrical coordinates. The influence of the grid resolution on the evolving flow morphology and propagation properties of supersonic HD and MHD jets was intensively analysed by Krause and Camenzind [35]. Their analyses was done by using the Newtonian MHD code NIRVANA, developed by Ziegler [64], which is a ZEUS type code.

A hydrodynamical light Mach 6 Jet is injected into a homogeneous ambient medium. Initially, the jet and the ambient medium are in pressure equilibrium $p_b = p_m$. The density ratio $\eta = \rho_b/\rho_m$ between the jet and the homogeneous medium was set to $\eta = 0.1$ with $\rho_m = 10$. The internal Mach number $M = v_b/cs_b$ of the jet was set to $M = 6$. Rotational symmetric boundary conditions are set at the jet axis, outflow at the right and upper boundary and reflecting at the left, except for the jet injection region, where inflow boundary conditions are set. This corresponds to the boundary conditions used by Krause. By setting the pressure to $p_b = 10^{-4}$ and the rest-mass density to $\rho_j = 1$ the problem is nonrelativistic in the thermodynamical sense and, since the beam velocity is given by $v_b = Mcs_b \ll 1$, also in the kinematical point of view. After the jet is

injected into the homogeneous ambient medium, a high pressure cocoon develops and interact with the supersonic beam. In the beam flow internal shocks are excited, leading to a time-dependent deceleration and re-acceleration of the beam. The evolved density structure, of the jet, is shown in Figure 4.1, for different grid resolutions of $10, 20, 40$ grid points (elements) per beam radius (ppb). The time is measured in light travelling units, where the unit-time scale is defined as the time the light needs to cross the jet radius, $[t] = R_j/c$, which is the natural time-scale for relativistic computations. Compared to the corresponding solution, setup B of Krause shown in Figure 3 in [35], the effective numerical resolution of this DG method seems to be about two times higher, than the effective resolution of the NIRVANA code. This behaviour is expected for codes based on Riemann solvers.

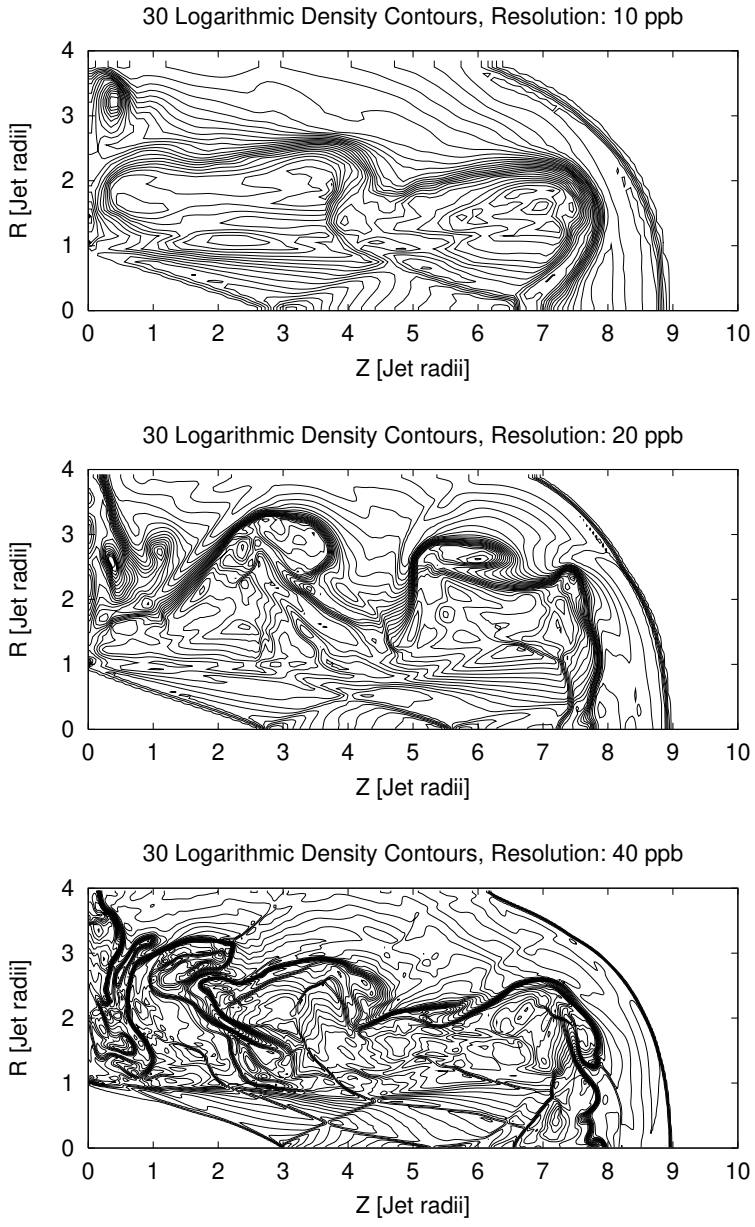

Figure 4.1: A Newtonian Mach 6 light Jet $\eta = 0.1$ for different resolutions (ppb points (elements) per beam radius), only the element mean values of the density are shown. Arrival times of the bow shocks at Z=9 R_b: $t_{ppb10} = 438.6$ $t_{ppb20} = 439.9$ $t_{ppb40} = 440.3$

4.1.2 Relativistic jets

The morphology and propagation properties of two-dimensional, axisymmetric relativistic jets was intensively analysed in the last years. For this problems Martí et al. [41], introduced a High Resolution Shock Capturing Scheme, which includes a Riemann solver for solving the relativistic Euler equation in conservation form. Duncan and Hughes [18] developed a relativistic code by using a second order Godunov-type solver. Now, there are also extensions to three-dimensional simulations of relativistic jets present, Hughes et al. [25] and Aloy et al. [1].

Relativistic jets differ from their Newtonian counterparts in two ways. The first is the dependence of the effective inertia $\rho h W^2$ on the flow velocity v_b and the specific internal energy ϵ, where ρ is the rest-mass density, $W = 1/\sqrt{1 - v_b^2}$ the beam Lorentz factor and $h = 1 + \epsilon + p/\rho$ the relativistic specific enthalpy. The second difference is the presence of a maximum velocity, the speed of light. In addition to the three parameters, the pressure contrast $\mathcal{K} = p_b/p_m$, density contrast $\eta = \rho_b/\rho_m$ and the beam Mach number M_b, which completely specify the propagation of Newtonian jets in homogeneous media, relativistic jets have to be specified by a fourth parameter, i.e., the beam velocity v_b or Lorentz factor W_b. Relativistic effects become important if large beam flow velocities $W_b \gg 1$ and/or high internal energies $h \gg 1$, compared to the rest mass energy, are involved. The pressure, for a gas with adiabatic index γ, is specified by the rest-mass density ρ_b, Mach number M_b and velocity v_b of the beam

$$p = \frac{c_s^2 \rho_b}{\gamma \left(1 - \frac{c_s^2}{\gamma - 1}\right)} \quad \text{with} \quad c_s = \frac{v_b}{M_b} \; . \tag{4.1}$$

For relativistic hot flows $h_b \gg 1$ the beam Mach number is bounded, since the sound speed is limited by the value $c_{s,max} = \sqrt{\gamma - 1}$ and has to be larger than

$$M_b > M_{min} = v_b / c_{s,max}. \tag{4.2}$$

To give an estimate of the dependence of the jet evolution properties on the beam Lorentz factor W_b and on the specific internal energy several cold jet simulations, models A in 4.1 with different rest mass density contrast η and three relativistic hot simulations, sign as models B in 4.1 were computed. The structure of rest mass density ρ and pressure p for the different cold jet models, for decreasing η are shown in the figures 4.8. The results of cold highly relativistic jets with Lorentz factor $W_b = 100$ are shown in the figures 4.15. The hot jet models are shown in figure 4.12. In addition two large scale runs for a cold and a hot jet model (LA2, LB) were computed to investigate the influence of the cocoon on the jet propagation. Regarding the results of model A1 (Fig. 4.2) , the influence of the Lorentz factor is dramatical. Although, the jet is less dense as the ambient medium $\eta = 0.1$ and a high pressure cocoon develops, but with less influence at this time on the beam flow. The propagation efficiency of the relativistic jet is quit higher compared to the Newtonian model N with corresponding initial data.

Propagation efficiency: To understand this property, the jet propagation efficiency in one dimension, defined as the velocity V_j of the working surface, is analysed. In the rest frame S' of the working surface which is moving with the velocity V_j relatively to the rest frame of the homogeneous ambient medium S, from the equation of local momentum conservation if initially a pressure equilibrium $p_b = p_m$ is assumed, Martí et al. [41], we get

$$\rho_b h_b \left(W_b' v_b'\right)^2 = \rho_m h_m \left(W_m' v_m'\right)^2 \ , \tag{4.3}$$

where v_b' and $v_m' = -V_j$ are the velocities of the beam and the ambient medium measured in S'. Transforming the beam velocity v_b, measured in S, into S' one gets

$$W_b' v_b' = W_j W_b \left(v_b - V_j\right) \tag{4.4}$$

and from this the jet propagation speed is parameterised by

$$V_j = \frac{\sqrt{\zeta}}{1+\sqrt{\zeta}} v_b, \tag{4.5}$$

where

$$\zeta = \eta \frac{h_b}{h_m} W_b^2 \tag{4.6}$$

is the effective inertial contrast which is the counterpart to Newtonian effective inertia given by the density ratio $\eta = \rho_b/\rho_m$. Therefore if $\zeta \gg 1$ the jet propagation efficiency is close to one, even if the jet is less dense as the ambient medium $\eta < 1$. Light jets $\eta < 1$ with a high propagation efficiency can be classified by two different types. The first type are highly kinematic $W_b \gg 1$ relativistic cold jets, with negligible internal energy, $h \approx 1$, and therefore hypersonic flows. The second type are hot jet, which are relativistic in the thermodynamic sense, where a large amount of the internal energy contributes to their total energy, $h \gg 1$.

Short distance runs: The grid resolution of the short distance runs was 20 ppb. The computational domain spans from 0 to 10 beam radii in the axial direction Z and from 0 to 4 beam radii in the radial direction R. The computation was stopped if the bow-shock reached $Z = 9R_j$ at the jet axis. The time was measured in light crossing times. The initial parameter of the different jet models (A,B) are listed in table 4.1. A comparison of the jet propagation efficiency is listed in table 4.2.

Cold jets $h \approx 1$: The cold jet models have beam Mach numbers much higher than the minimum beam Mach number given by Eq. 4.2, $M_b \gg M_{min}$. Cold jet are, therefore, supersonic. In figure 4.2 the resulting rest-mass density of model A1 and his Newtonian counterpart are shown. The rest-mass density ratio of both jet is initially $\eta = 0.1$ and a equal beam Mach number $M_b = 6$.

Only the beam Lorentz factor was changed, from $W_b \approx 1.003$, for the Newtonian jet, to $W_b = 10$ for the relativistic model. Visible is the decreasing influence of the high pressure cocoon on the internal beam structure, by increasing beam Lorentz factor W_b. In the Newtonian model internal shocks are excited, leading to a deceleration and re-acceleration of the beam. The appearance of Kelvin-Helmholtz instabilities, leads to a mixing of the shocked ambient medium and back flowing beam matter. Whereas by increasing beam Lorentz factor these instabilities have not enough time to disturb the cocoon. By decreasing the rest-mass density ratio, model A2, with $\eta = 0.01$, and model A3, $\eta = 0.001$ the influence of the high pressure cocoon on the internal beam increases.

Hot jets $h \gg 1$: The Mach number of the hot jet models (Setups B in table 4.1) is approximately that of the minimum beam Mach number, Def. 4.2. These models are therfore low Mach number jets. In the case of hot jets, the beam and cocoon are nearly in pressure equilibrium (right contour plots of figure 4.12). This leads to a reduced influence of the cocoon on the propagating beam. In addition the back-flowing of shocked ambient material is suppressed and no Kelvin-Helmholtz instabilities are visible at this time. Only in model B1, where the rest-mass density ratio is $\eta = 0.001$ strong internal shocks are formed. But in comparison to the cold model A3 with equal initial states except of the Mach number, the cocoon is less dominant and the propagation speed of model B1 is approximately three times higher than that of the cold model.

Long distance runs: The computational domain of the long distance runs spans to 50 jet radii in the axial direction and to 10 in the radial direction. The resolution was set to 10 elements per beam radius for $R < 7$. For Radii larger than $R > 7$ the radial element size was geometrical increased, to reduce the influence of the upper outflow boundary on the simulations.

In the long term runs the influence of the internal energy on the jet morphology is visible. The cold jet simulation LA2 shown in Fig. 4.16 develops a pressure dominated cocoon with back-flowing beam material, leading to Kelvin-Helmholtz instabilities at the contact surface and a mixing of the cocoon and shocked ambient medium. In the cocoon shocks are developed, leading to dissipation of the kinematical energy of the back-flowing beam material, which heats the cocoon far a way of the bow-shock. Further the higher pressure cocoon influence the beam and internal shocks are arising, which decelerate and re-accelerate the beam. In contrast to the properties of the cold model, the hot jet model LB, Fig. 4.17, no dominant cocoon with back-flowing beam material is developed. Since the beam and cocoon is approximately in pressure equilibrium, internal shocks are suppressed and the jet propagates nearly in a one-dimensional fashion. These results are in agreement with the computations of Martí et al. [41].

Model	Type	$\eta = \rho_b/\rho_m$	W_b	M_b	$\mathcal{M}_b$	$\zeta = W_b^2 \eta h_b/h_m$	ppb
A1	Cold	0.1	10	6	59.17	≈ 10	20
A2	Cold	0.01	10	6	59.17	≈ 1	20
LA2	Cold	0.01	10	6	59.17	≈ 1	10
A3	Cold	0.001	10	6	59.17	≈ 0.1	20
A4	Cold	0.1	2	6	11.87	≈ 0.4	20
A5	Cold	0.01	100	6	591.6	≈ 104	20
A6	Cold	0.001	100	6	591.6	≈ 10.4	20
B1	Hot	0.001	10	$1.020 \times M_{min}$	7.45	≈ 2.5	20
B2	Hot	0.01	2	$1.015 \times M_{min}$	1.28	≈ 1	20
B3	Hot	0.01	10	$1.020 \times M_{min}$	7.45	≈ 20.6	20
LB	Hot	0.01	10	$1.020 \times M_{min}$	14.49	≈ 20.6	10

Table 4.1: Initial physical parameters for the different models with proper rest mass ratio $\eta = \rho_b/\rho_m$, beam Lorentz factor W_b and effective inertial ratio $\zeta = W_b^2 \eta h_b/h_m$. The adiabatic index was set to $\gamma = 5/3$, except for the hot long evolution model LB, where the adiabatic index was set to $\gamma = 4/3$. The minimum Mach number $M_{min} = v_b/c_{s_{max}}$, where the maximal reachable sound speed, if $P \gg \rho$, is given by $c_{s_{max}} = \sqrt{\gamma - 1}$ and the proper Mach number is given by $\mathcal{M}_b = M_b W_b/W_s$, where $W_s = 1/\sqrt{1 - c_s^2}$ is Lorentz factor of the sound speed. The grid resolution (ppb) is measured by points (elements) per beam radius R_j.

Model	Type	ζ	V_j^N	V_j	$\bar{v}_j$	δ	δ_N	t_{end}
A1	Cold	10	0.239	0.759	0.789	1.040	3.30	11.0
A2	Cold	1	0.090	0.503	0.5	0.995	5.55	16.4
LA2	Cold	1	0.090	0.503	0.44	0.852	4.89	112.1
A3	Cold	0.1	0.031	0.243	0.199	0.821	6.42	39.1
A4	Cold	0.4	0.208	0.338	0.352	1.040	1.69	23.3
A5	Cold	104	0.091	0.911	0.931	1.022	10.2	9.13
A6	Cold	10.4	0.031	0.764	0.765	1.002	24.7	11.0
B1	Hot	2.5	0.031	0.610	0.594	0.974	19.2	13.8
B2	Hot	1	0.079	0.435	0.325	0.746	4.11	16.0
B3	Hot	20.6	0.090	0.815	0.820	1.005	9.11	10.1
LB	Hot	20.6	0.090	0.815	0.813	0.997	8.99	60.27

Table 4.2: Comparison of propagation efficiency between the 1D analytic and the simulations for the different jet models, where models LA2 and LB are long evolution runs, jet propagation to $Z = 49\ R_j$. Here ζ is the effective inertial contrast, V_j^N is the Newtonian and V_j is the relativistic one dimensional estimate of the propagation velocity of the contact discontinuity (working surface) and $\bar{v}_j$ is the average velocity obtained from the simulations. The propagation efficiency of the jet is defined by the ratio $\delta = \bar{v}_j/V_j$ of the two-dimensional computed jet mean propagation velocity $\bar{v}_j$ compared to the one-dimensional estimate V_j given by Eq. 4.5. The ratio of the Newtonian jet propagation velocity V_j^N and the two dimensional propagation velocity is defined by $\delta_N = \bar{v}_j/V_j^N$. t_{end} is given by the time the bow shock needs to reach $Z = 9\ R_j$, except for the model LA2 and LB, where $Z = 49\ R_j$.

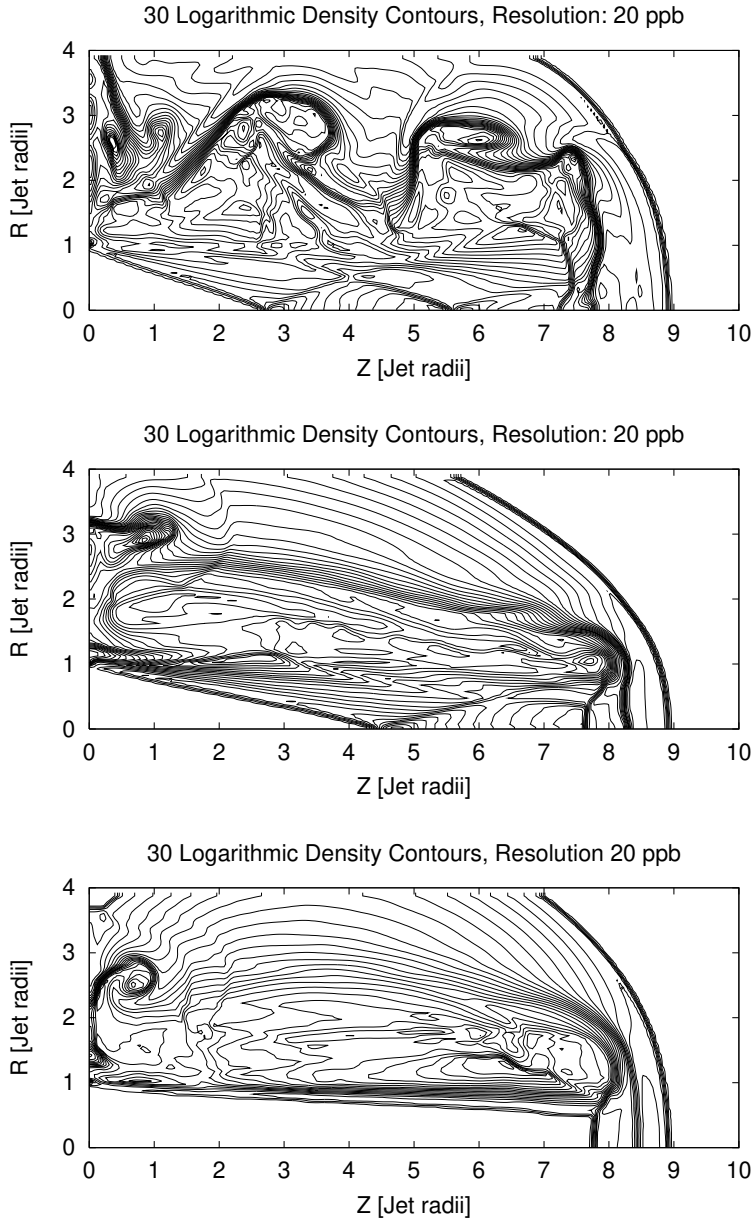

Figure 4.2: Jet model (N, A4, A1): 30 equal spaced contours of the logarithm of rest mass density ρ for the Mach 6 jet models (N, A4, A1), with rest-mass density ratio $\eta = 0.1$ by increasing beam Lorentz factor W_b from top to down. The Newtonian jet has a beam Lorentz factor $W_b \approx 1.003$, the mildly relativistic $W_b = 2$ and the relativistic $W_b = 10$. The arrival times of the bow shocks to reach $Z = 9R_b$ are for the Newtonian jet $t \approx 440$, for the mildly relativistic $t = 23.3$ and for the relativistic jet model $t \approx 10.97$

Figure 4.3: N

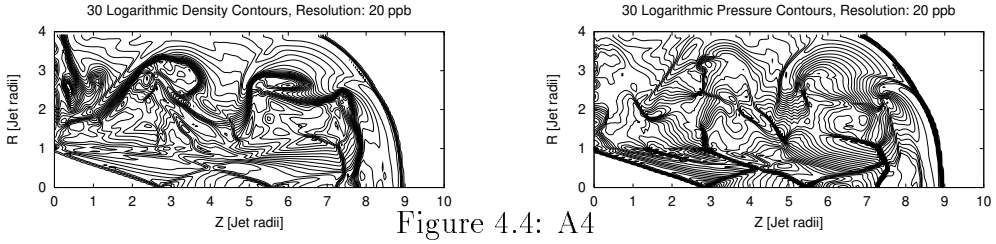

Figure 4.4: A4

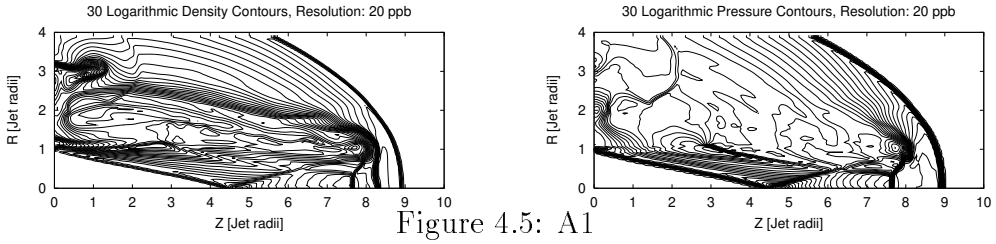

Figure 4.5: A1

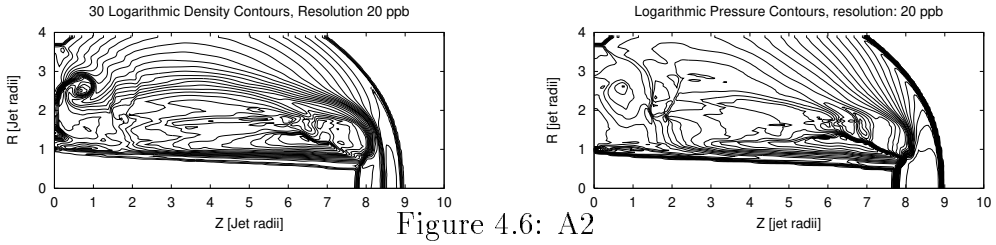

Figure 4.6: A2

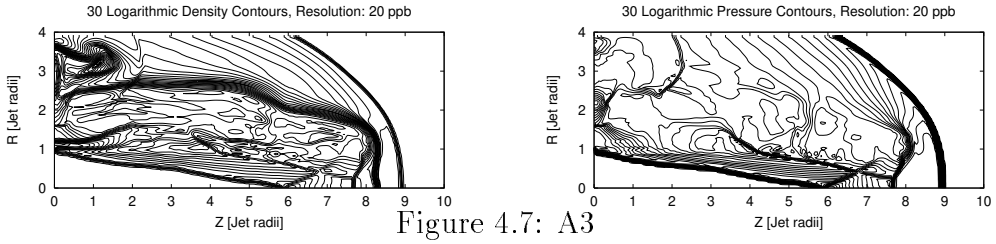

Figure 4.7: A3

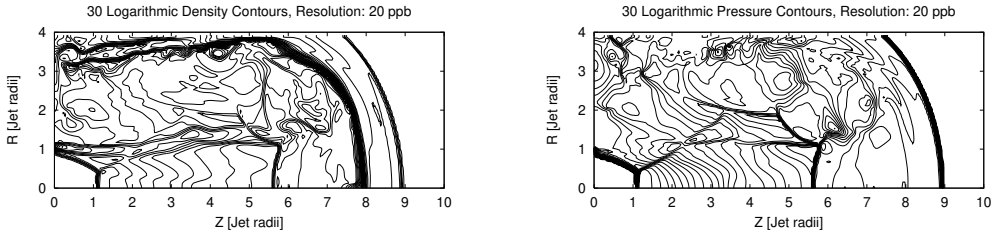

Figure 4.8: Cold jet models A: Rest mass density ρ and pressure p of the different cold jet models with beam Mach number $M_b = 6$. The first three panels, from top, showing the resulting flow pattern for the Newtonian jet $W_b \approx 1.003$, the mildly relativistic model A4 with $W_b = 2$ and the relativistic model A1 $W_b = 10$ with rest mass density contrast $\eta = 0.1$. The two lower panels are the results of models A2 and A3 for increasing density contrast $\eta = 10^{-2}, 10^{-3}$. The different initial parameters are listed in table 4.1 and propagation efficiency and time scale in table 4.2.

Figure 4.9: B1

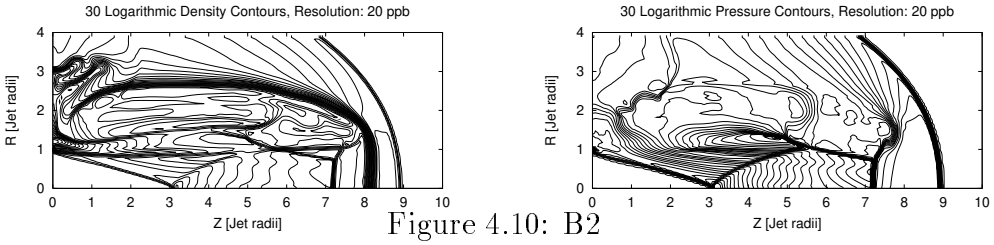

Figure 4.10: B2

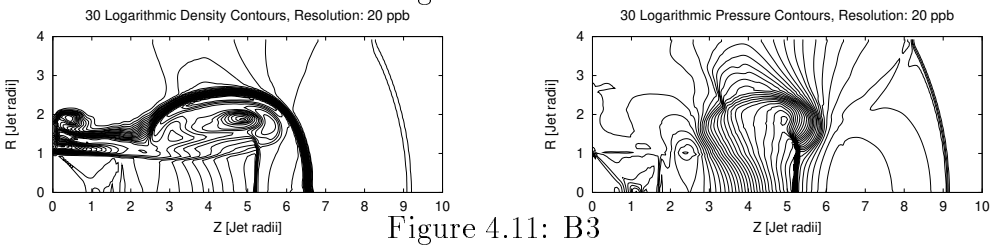

Figure 4.11: B3

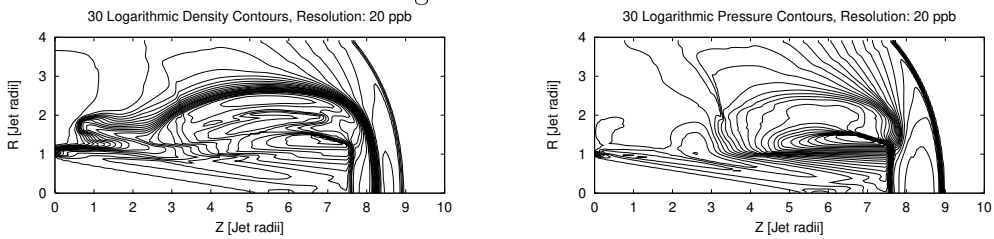

Figure 4.12: Hot jet models B: Contour plots of rest mass density ρ and pressure p of the different hot low beam Mach number $M_b \approx M_{min}$ jet models. The models from the top are B1,B2 and B3. The different initial parameters are listed in table 4.1 and propagation efficiency and time scale in table 4.2.

Figure 4.13: A5

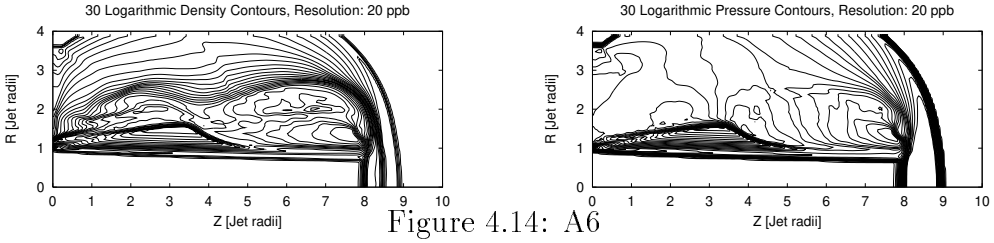

Figure 4.14: A6

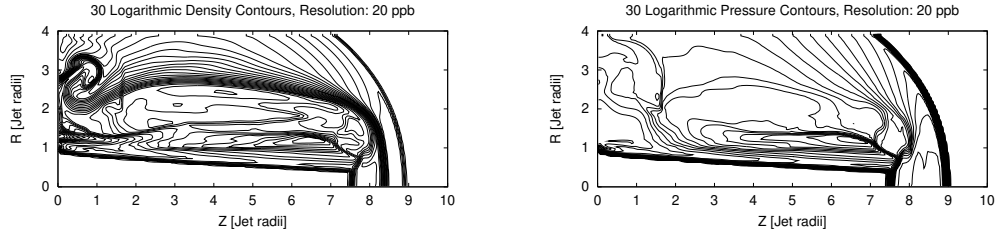

Figure 4.15: Cold high relativistic jet models (A5,A6) $W_b = 100$: Contour plots of the logarithm of rest mass density ρ and pressure p.

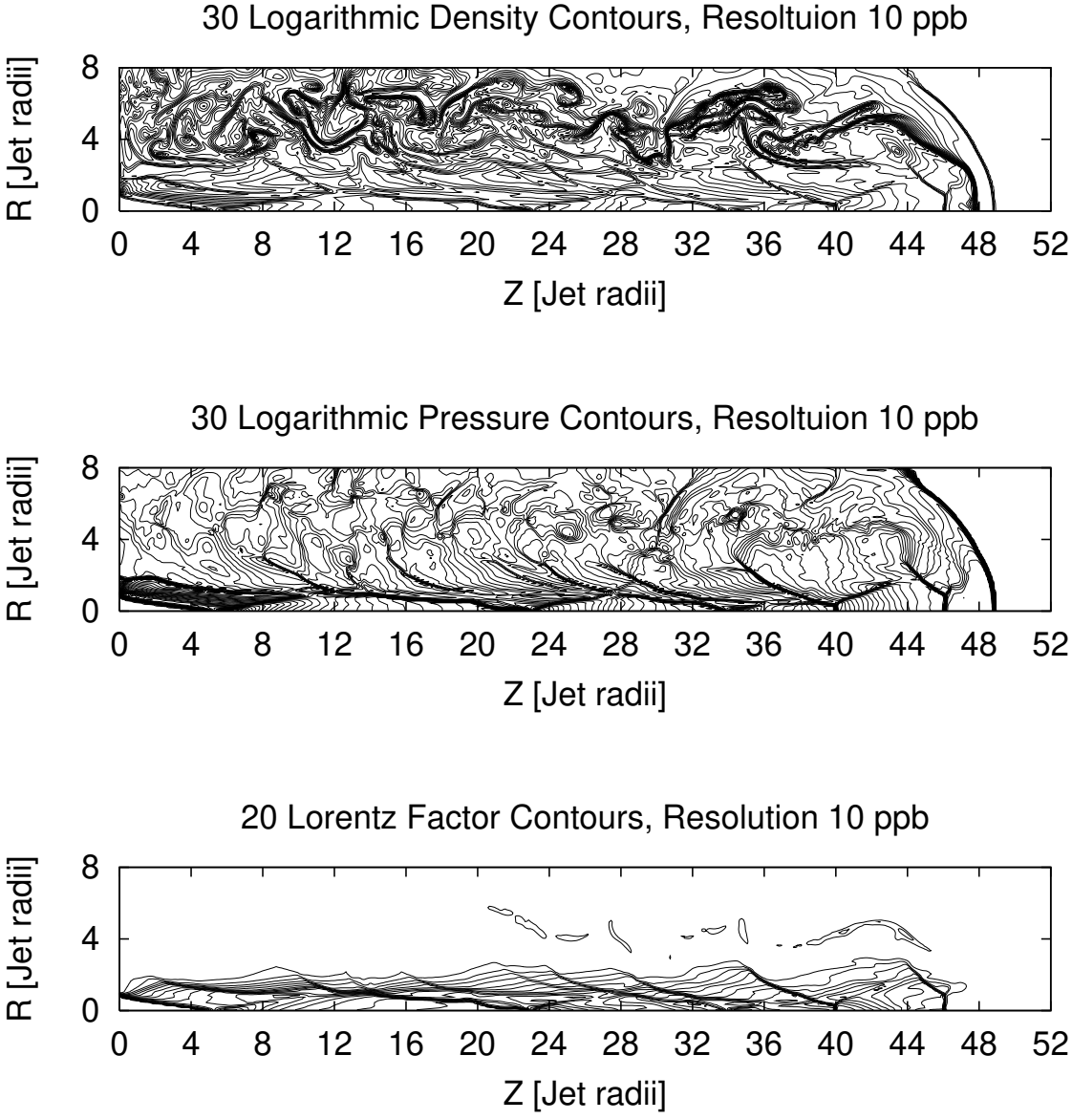

Figure 4.16: Long evolution run of the jet model LA2 at time $t = 112.1$

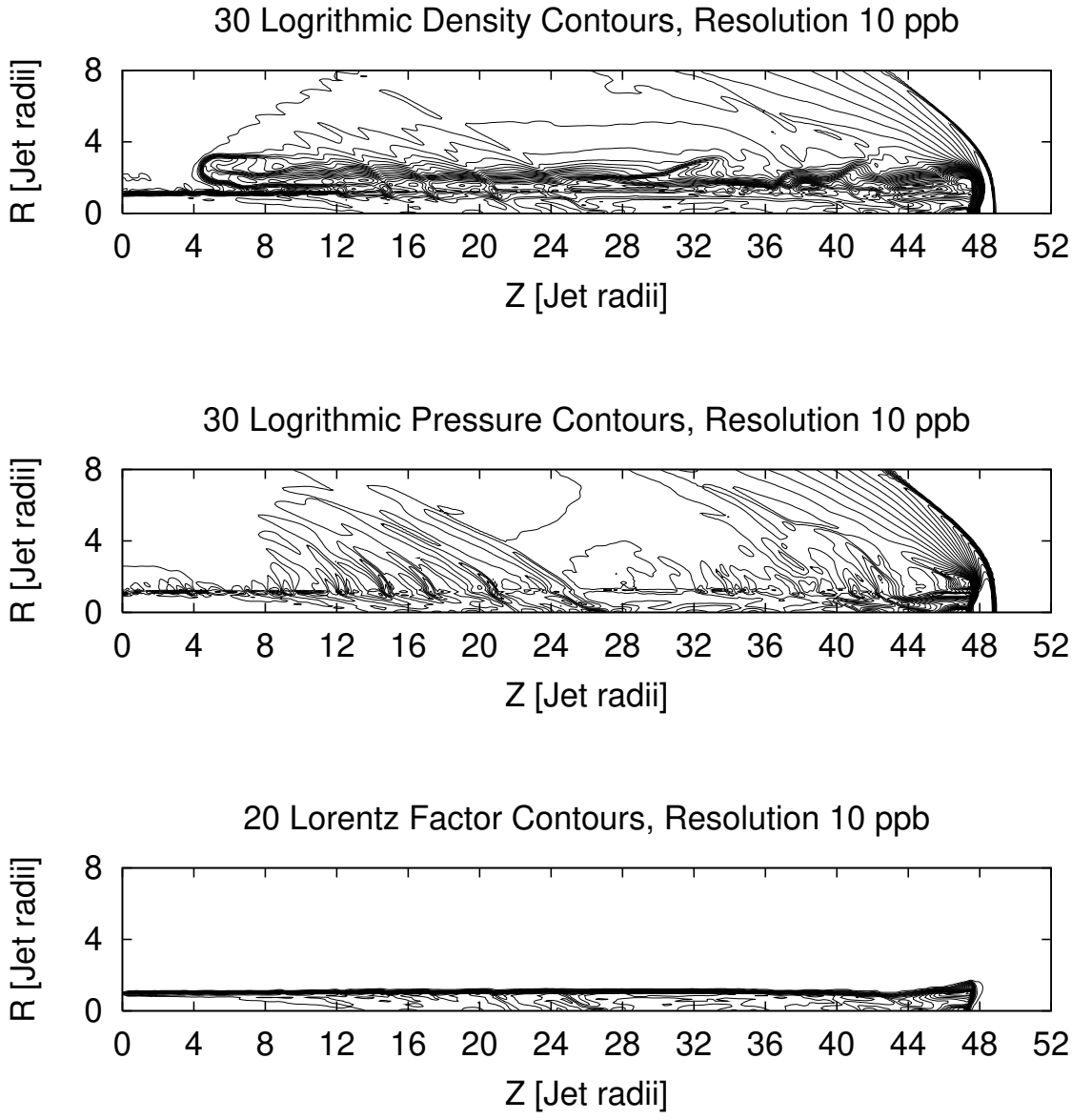

Figure 4.17: Long evolution run of the jet model LB at time $t = 60.27$

4.2 Spherical Bondi accretion in the Schwarzschild spacetime

In this section the code is tested on the one-dimensional accretion models of Bondi for transonic stationary flows in the metric of a non-rotating Black Hole with gravitational mass M. New source terms, from the gravitation and coordinates are involved. The time is measured in light-crossing times $t_g = r_g/c$, where the gravitational radius is given by r_g. The Schwarzschild radius is give by $r_{E.H.} = 2r_g$. At first it was investigated if the code is able to keep an analytic solution stationary. This was done by using the analytical solution as initial data and evolving over the typical times scales, the free-fall time $t_{ff} \approx \sqrt{2/r_{out}^3}$. In the second test the code has to find the true solution by advection of the appropriate boundary conditions inwards. Following Hawley et al. [21] the stationary transonic solution of an adiabatic, $\rho \propto T^n$, with $T = P/\rho = (\gamma - 1)$ and $n = 1/(\gamma - 1)$, accretion flow is derived from the particle number conservation

$$\partial_r \left(\sqrt{-G} D v^r \right) = \partial_r \left(r^2 \rho U^r \right) = 0. \tag{4.7}$$

Therefore, the mass accretion rate

$$r^2 \rho U^r = C_1 \tag{4.8}$$

is a constant of motion and, from the energy conservation,

$$\partial_r \left(\alpha \sqrt{-G} (E + p) v^r \right) = \partial_r \left(\alpha r^2 \rho U^r h W \right) = 0 \ , \tag{4.9}$$

it follows that the energy accretion rate

$$\alpha r^2 \rho h W U^r = C_2 \tag{4.10}$$

is also a constant of motion. By the definition

$$C_3 = \left(\frac{C_2}{C_1} \right)^2 = (\alpha W h)^2 = \alpha^4 h^2 U^{t\,2} \ , \tag{4.11}$$

since $U^t = W/\alpha$ and by using the normalisation of the four velocity $g_{\mu\nu} U^\mu U\nu = -1$ the time component of the four velocity is then given by $U^{t\,2} = \left(1 + g_{rr} (U^r)^2\right) / g_{tt}$. Like in Hawley et al. [21] the sonic radius r_s is selected to determine the constants of motion, C_1 and C_2.

The initial states of the first test problem are given by the analytical solution of an initial transonic flow with critical point at $r = 30 r_g$. The radial range was $r \in [2.5, 110]$ with 100 non-equally spaced elements. After the evolution time $t = 2000 \approx 2.8 t_{ff}$, some influence from the boundaries are visible in the results (Fig.4.18), but the code remain close to the analytical solution. A quite lower grid resolution run, of 50 non-equally spaced elements in the range $2.5 < r <$

2.25×10^3, with sonic radius at $10r_g$ was computed, till $t = 10^4[t_g]$. In figure 4.19 the numerical results are compared to the analytical solution. In the third test problem the code has to find the true solution by advection of the appropriate boundary values inwards. 50 non-equally spaced elements in the radial range $2.5 < r < 92$ were used. After the evolution time $t = 8.0 \times 10^3$ the analytical solution is nearly reached, as shown in Fig. 4.20.

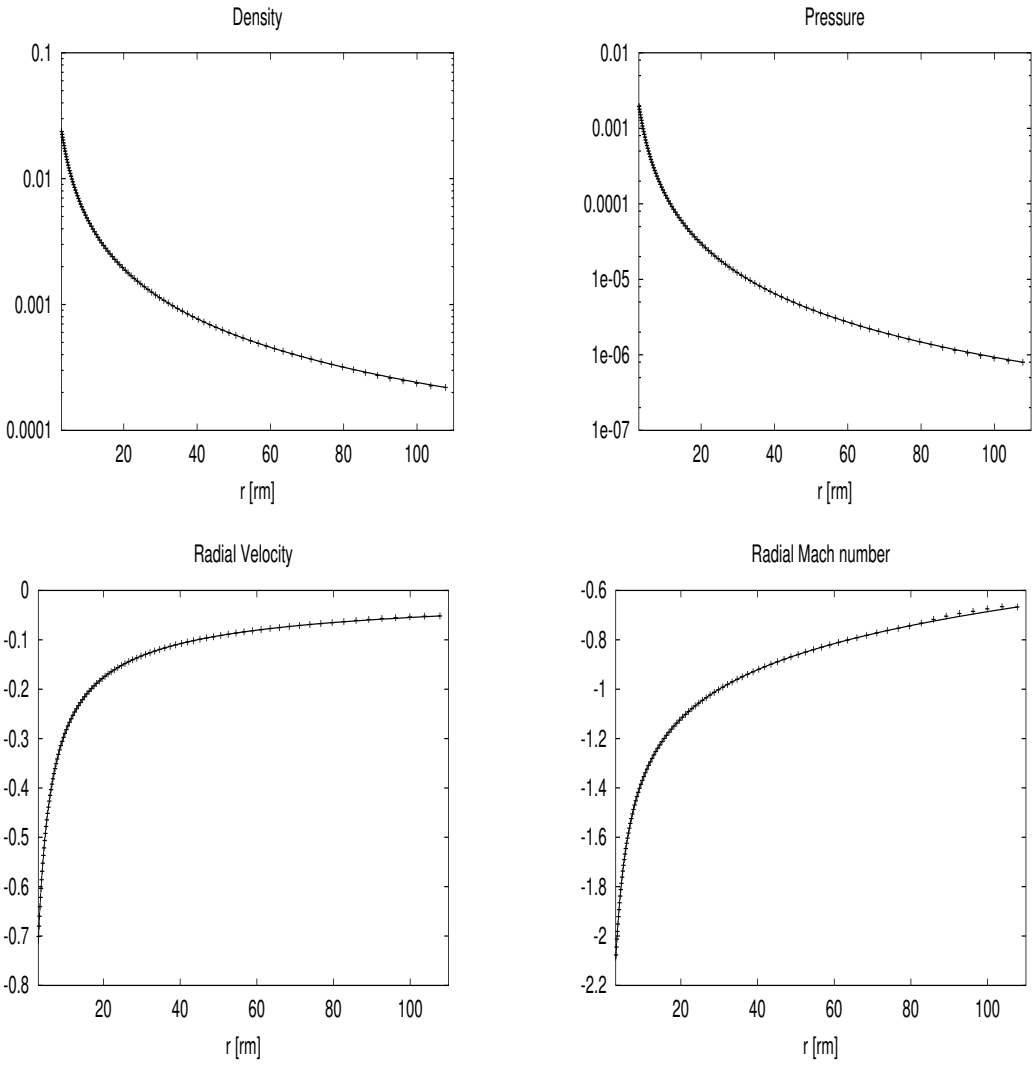

Figure 4.18: The states of a stationary relativistic Bondi accretion model with sonic radius $r_s = 30r_g$. Shown are the analytic solutions (solid lines) and the numeric solutions at time $t = 2000[t_g]$. Some influence of the boundary is visible in the figures.

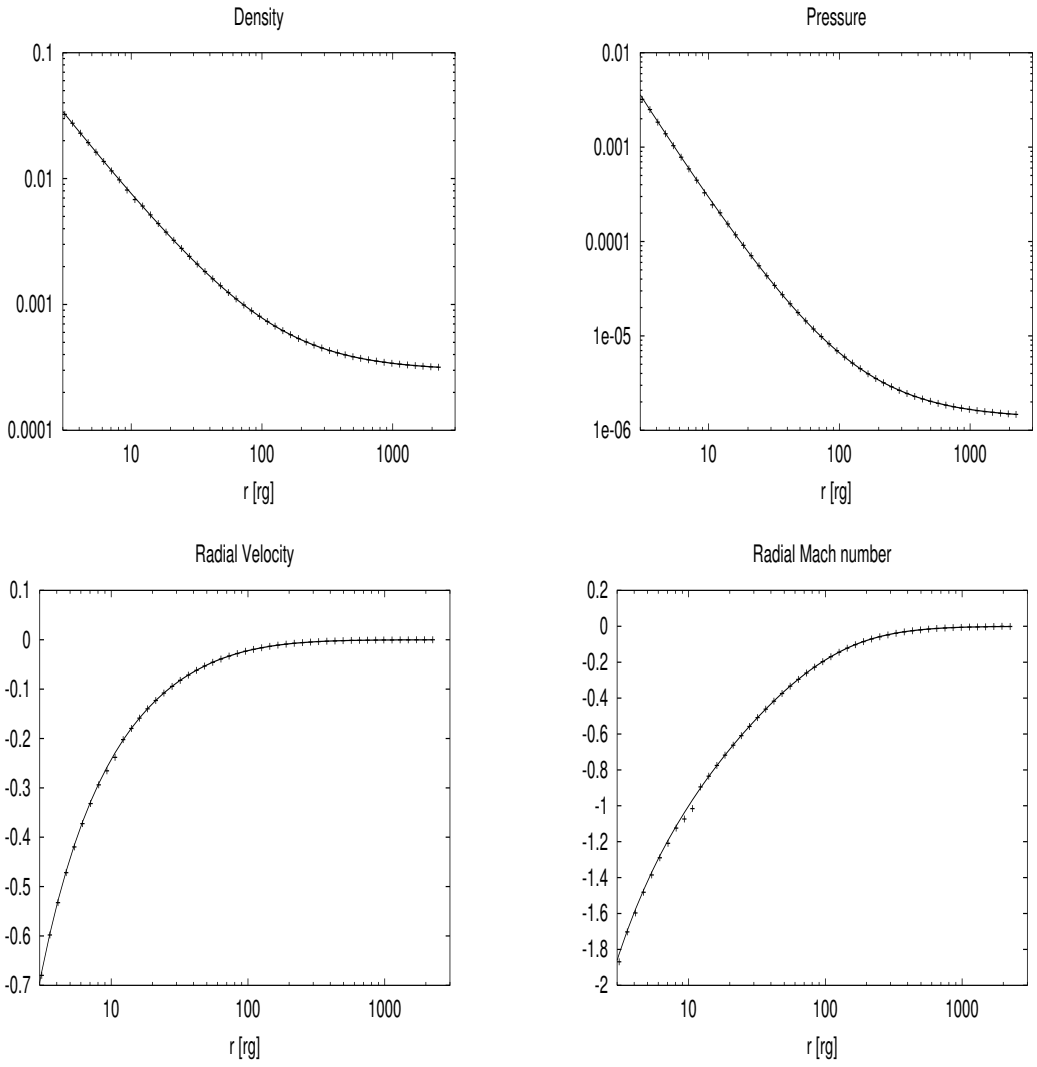

Figure 4.19: The states of a stationary relativistic Bondi accretion model with sonic radius $r_s = 10r_g$. Shown are the analytic solutions (solid lines) and the numeric solutions at time $t = 10^4[t_g]$

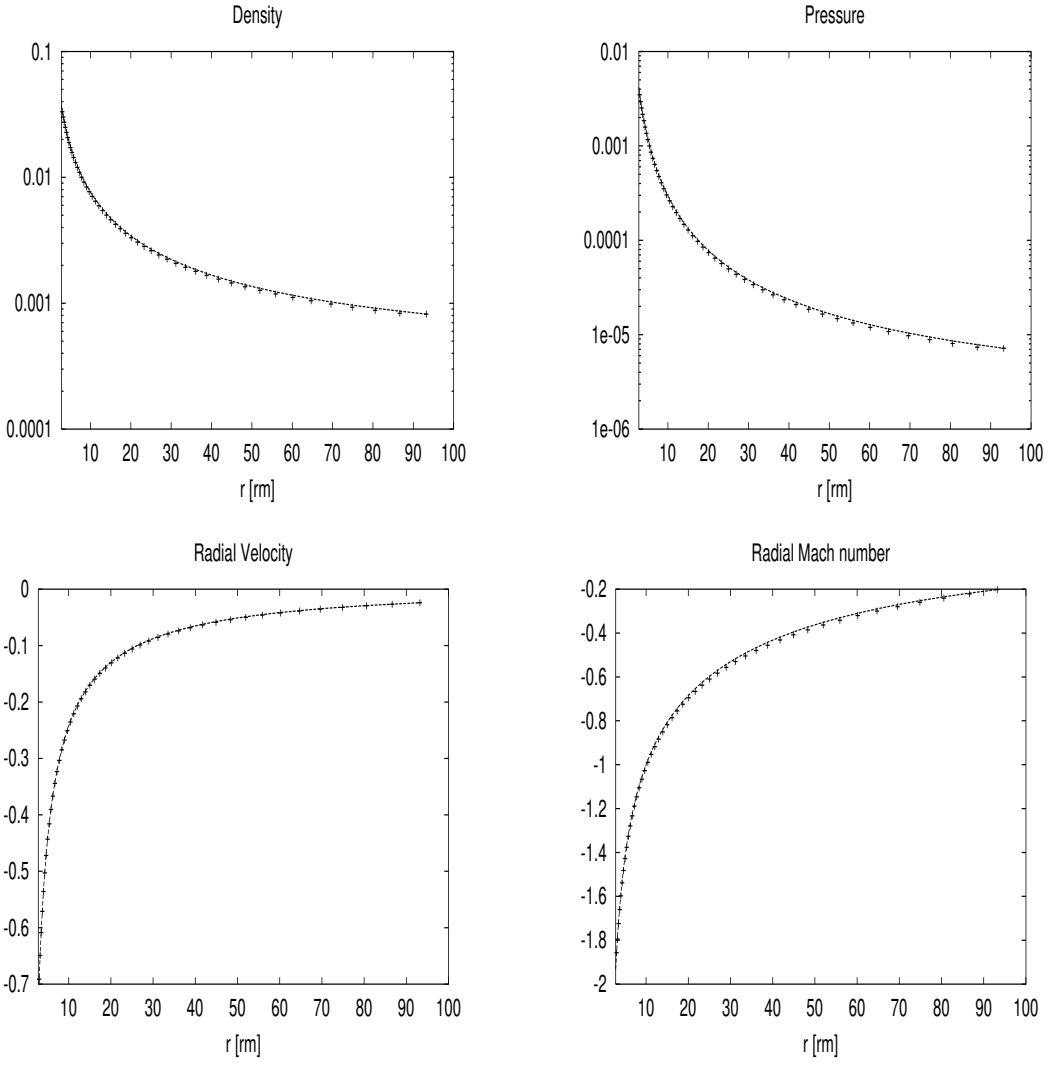

Figure 4.20: Time-dependent test problem: Advection from the outer boundary. The states of a stationary relativistic Bondi accretion model with sonic radius $r_s = 10r_g$. Shown are the analytic solutions (solid lines) and the numeric solutions at time $t = 8 \times 10^3\,[t_g]$.

4.3 A relativistic Keplerian accretion disc in 2.5D

In this section we apply the code to a model of a relativistic Keplerian disc in the stationary Schwarzschild metric, by neglecting self-gravity of the disc, $M_{disc} \ll M_{BH}$. This problem was also tested by Koide et al. [30]. The space and time units are given by the gravitational radius r_g and the light-crossing time $t_g = r_g/c$. The computational domain was discretised by 80×80 elements. The computational mesh was uniformly spaced in θ direction, from $-\pi/2 \leq \theta \leq \pi/2$, where the equatorial plane is at $\theta = 0$. In the radial direction the mesh ranges from $r_{in} = 2.4\ r_g$ to $r_{out} = 50\ r_g$ with non-equally spaced elements $\Delta r = \sqrt{g_{\theta\theta}/g_{rr}}\Delta\theta$. At both axis of symmetry, $\theta = -\pi/2$ and $\theta = \pi/2$, rotational symmetric boundary conditions were set. At the inner boundary r_{in} we set outflow conditions and at the outer boundary r_{out} inflow conditions.

Initial conditions: Initially the disc rotates with the Keplerian velocity

$$v_K = \frac{1}{\sqrt{2(\frac{1}{2}r - 1)}}$$

and was surrounded by a hot stationary accreting Bondi solution of section 4.2 with the sonic-radius $r_s = 4r_g$ and states $\rho_C(r)$, $v_C(r)$, $p_C(r)$. The adiabatic index of the gas was set to $\gamma = 5/3$. This accreting corona was supersonic for radii smaller than r_s. The inner disc radius r_D was set to the radius of the marginal-stable orbit $r_{m.s.} = 6r_g$. Therefore, initially there exists a gap between the event horizon and the disc. The disc height scales initially with $H_D(r) = 0.1r$. The initial data for the velocities are

$$(v_r, v_\theta, v_\phi) = \begin{cases} (v_C, 0, 0) & \text{if } r < r_D \text{ and } |z| > H_D(r) \\ (0, 0, v_K) & \text{if } r \geq r_D \text{ and } |z| \leq H_D(r) \end{cases} \tag{4.12}$$

and for the density

$$\rho(r, \theta) = \begin{cases} \rho_C(r) & \text{if } r < r_D \text{ and } |z| > H_D(r) \\ \rho_D = \rho_C(r) f(z) & \text{if } r \geq r_D \text{ and } |z| \leq H_D(r) \end{cases}, \tag{4.13}$$

with $f(z) = 100e^{-z/h_s}$ and scale height $h_s = 0.6r_g$. At the equator, $\theta = 0$, the density of the disc, ρ_D, was therefore 100 times the density of the corona, ρ_C. The global pressure was set to that of the corona

$$p(r, \theta) = p_C(r). \tag{4.14}$$

Results: Initially the disc was not in a hydrostatic equilibrium. At the beginning, $t > 0$, the matter of the corona falls fast into the black hole. The region of the gap between the horizon and the disc can not be fed fast enough by the

ambient matter and is rarefied. This leads to a pressure decrease in this region. Driven by this pressure gradient, at the inner disc boundary, the inner part of the disc falls slightly inwards. Further, at the same time, there is a pressure gradient present in the disc, since initially $p_D = p_C(r)$, which accelerates the outer part of disc matter further outwards. These circumstances leads to a excitation of pressure and density waves inside the disc, which are moving to larger disc radii. These waves also interacts with the accretion corona. A quasi stationary state was reached after approximately four rotational periods of the inner disc. In figure 4.21 the rest mass density measured in the rest frame of the fluid and the velocities measured in the frame of the Zero Angular Momentum Observers (ZAMOs) are shown after ≈ 5.5 Keplerian rotations of the inner disc. The excited density and pressure wave in the disc and their interaction with the accretion corona are visible.

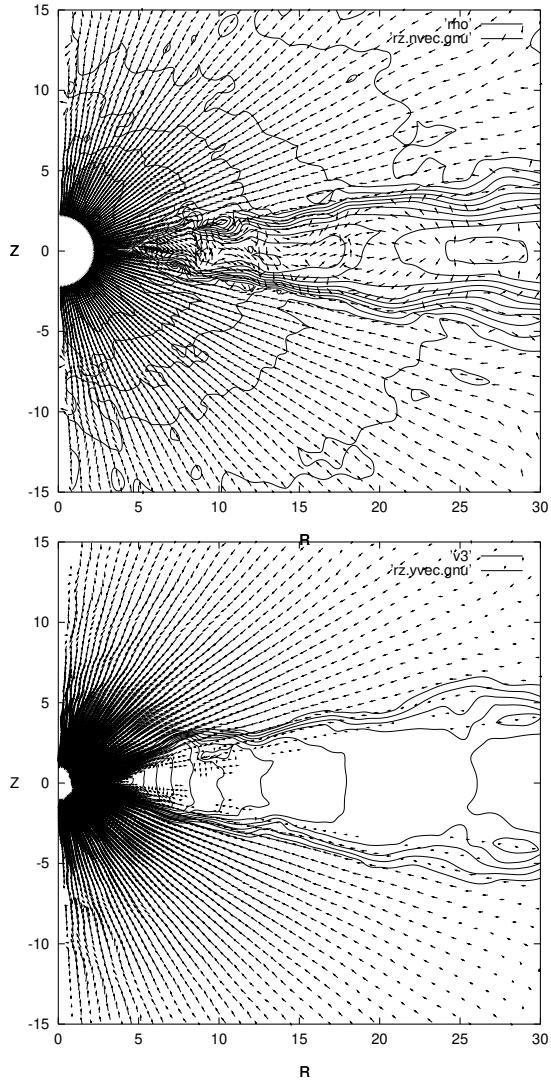

Figure 4.21: The Keplerian disc after 5.5 Keplerian rotations at the radius $r_{ms} = 6\ r_g$ of the marginal stable orbit: In the upper figure the isolines of the logarithm of proper rest mass density ρ and normalised poloidal velocity vectors are shown. The lower figure shows the isolines of the rotation velocity $v_{\hat{\phi}} = r\omega$ and the poloidal velocity vectors, measured by the ZAMOs.

Chapter 5

Discussion

What has been done. In this work we have developed a new time-explicite code for solving the time-dependent problems of the ideal relativistic hydrodynamics in two dimensions. The equations are solved in their conservative form of the 3+1 split of spacetime. The code can solve the conservation laws in Cartesian, cylindrical, spherical coordinates and in the spherical Schwarzschild metric. The spatial discretisation scheme is based on the Discontinuous Galerkin Method for nonlinear hyperbolic conservation laws, introduced by Cockburn and Shu [13] for the Newtonian Euler equation. This is a stable Finite Element method with high accuracy even on unstructured meshes. The spatial order of accuracy is given by the order of the discontinuous Finite Element basis. Since the coupling between the computational sub-domains is not influenced by the FE basis, the method remains compact, independent of the spatial order of accuracy. Only the fluxes between the connecting sub-domains have to be computed. This property is of advantage for the implementation on parallel computers. To get a stable second or higher order method, a slope limiting of the conservative variables has to be applied. If the slope limiting is applied on the characteristic variables, by using the Total Variation Bounded (TVB) minmod limiter, a high resolution method is achieved in more than one dimensions, even without the use of approximate or exact Riemann solvers. The code solved successfully a variety of Newtonian and relativistic test problems in one and two dimensions. We conclude that the effective numerical resolution for the piecewise linear element basis P^1 is between the resolution of the second order MUSCL scheme and the resolution of the piecewise parabolic method (PPM). This conclusion only holds if the surface and volume integrals are numerically evaluated with the appropriate order for the exact integration of the polynomial order of the basis functions.

We applied the code on the astrophysical problem of the relativistic jet propagation through an homogeneous ambient medium. In the short-scale runs a variety of axisymmetric jet models was studied. To compare the long-term evolution of a light cold jet and a relativistic hot jet two larger scale runs were simulated. The results are in agreement with the results obtained by other high

resolution schemes.

The time-dependent evolution of a Keplerian disc in the Schwarzschild background-metric was studied. The simulation runs over several rotations of the inner disc boundary, which was initially located at the marginal stable radius of six gravitation radii. The disc was initially surrounded by a stationary hot accreting Bondi solution, which was supersonic for radii lower than four gravitational radii. Since these initial conditions are not really stationary a small amount of disc matter is accreted into the Black Hole. In addition, oscillations are excited in the disc, which are interacting with the surrounding hot accretion corona. A quasi steady solution was reached after approximately four rotations of the inner disc.

Future work: In the numerical point of view, to reduce the computational effort an Adaptive Mesh Refinement (AMR) method should be included, as well as a parallelisation of the code is useful. From the physical point of view, the equations of magnetohydrodynamics have to be included, since in a large range of astrophysical problems magnetic fields are relevant for the dynamics. This happens for example in the problem of the jet formation, where magnetic fields are believed to be the engine for the acceleration and collimation of the jets. Further, the coupling between magnetic fields and the fluid influence the angular momentum transport in accretion discs. Also the inclusion of dissipative effects of non-ideal fluids, like viscosity and radiative cooling is needed for the simulation of more realistic models of accretion discs. The Müller-Israel-Stewart theory of causal thermodynamics include a finite propagation speed for viscous and heat signals. This property is more physical than the infinite signal speeds of the classical theory of non-ideal hydrodynamics, especially, if relativistic velocities are involved. Peitz and Appl [49] have formulate the theory of dissipative relativistic hydrodynamics in the formalism of the 3+1 split of spacetime. These equations should be numerically solvable if modern high resolution methods are applied. Since the characteristic fields of these equations are complicate, a method which is not based on Riemann solvers seems to be rather efficient to solve this problem.

Appendix A

Characteristic fields of the ideal relativistic hydrodynamic conservation laws

In this appendix the characteristic fields of the homogeneous part

$$\frac{\partial \mathbf{U}}{\partial t} + \frac{\partial \mathbf{F^k}(\mathbf{U})}{\partial x^k} = \mathbf{0} \tag{A.1}$$

of the ideal relativistic conservation laws are reviewed. The left and right eigenvectors and the corresponding eigenvalues are explicitly shown, needed for the slope limiting of the characteristic variables and for the use of the Marquina flux splitting. The notation follows the report of Aloy et al [1]. The analytical expression for the corresponding characteristic decomposition

$$\mathbf{A} = \mathbf{R}\mathbf{\Lambda}\mathbf{R^{-1}} \tag{A.2}$$

of the 5×5 Jacobian matrix

$$\mathbf{A}^i = \frac{\partial \mathbf{F}^i(\mathbf{U})}{\partial \mathbf{U}} \tag{A.3}$$

of the fluxes $\mathbf{F}^i(\mathbf{U})$ was elaborated by Donat et al. [16]. The characteristic fields are explicitly shown for $\mathbf{A}^x$, whereas the cases y and z follows from symmetry. The eigenvalues are

$$\lambda_\pm = \frac{1}{1 - v^2 c_s^2}\left(v^x\left(1 - c_s^2\right) \pm c_s\sqrt{(1-v^2)\left[1 - v^x v^x - c_s\left(v^2 - v^x v^x\right)\right]}\right) \tag{A.4}$$

and

$$\lambda_0 = v^x \ . \tag{A.5}$$

The matrix of eigenvalues $\mathbf{\Lambda}$ is then given by

$$\mathbf{\Lambda} = \mathrm{diag}\left[\lambda_-, \lambda_0, \lambda_0, \lambda_0, \lambda_+\right], \tag{A.6}$$

which reduces for small velocities $v^i \ll 1$ and small internal energies compared to the rest mass energy to the Newtonian form $\mathbf{\Lambda} = \mathrm{diag}\left[v^x - c_s, v^x, v^x, v^x, v^x + c_s\right]$. The upper bound of the eigenvalues is given by the speed of light, $|\lambda_l| < 1$. By defining the quantities:

$$\tilde{\kappa} = \frac{1}{\rho}\frac{\partial p}{\partial \epsilon}\bigg|_{\rho} \quad , \mathcal{K} \equiv \frac{\tilde{\kappa}}{\tilde{\kappa} - c_s^2} \; , \mathcal{A}_{\pm} \equiv \frac{1 - v^x v^x}{1 - v^x \lambda_{\pm}}, \tag{A.7}$$

the right eigenvectors are

$$\mathbf{r}_{\pm} = \left(1, hW\mathcal{A}_{\pm}\lambda_{\pm}, hWv^y, hWv^z, hW\mathcal{A}_{\pm} - 1\right), \tag{A.8}$$

$$\mathbf{r}_1 = \left(\frac{\mathcal{K}}{hW}, v^x, v^y, v^z, 1 - \frac{\mathcal{K}}{hW}\right), \tag{A.9}$$

$$\mathbf{r}_2 = \left(Wv^y, 2hW^2 v^x v^y, h\left(1 + 2W^2 v^y v^y\right), 2hW^2 v^y v^z, 2hW^2 v^y - Wv^y\right), \tag{A.10}$$

$$\mathbf{r}_3 = \left(Wv^z, 2hW^2 v^x v^z, 2hW^2 v^y v^z, h\left(1 + 2W^2 v^z v^z\right), 2hW^2 v^z - Wv^z\right), \tag{A.11}$$

which are the columns of the matrix

$$\mathbf{R} = \left[\mathbf{r}_-|\mathbf{r}_1|\mathbf{r}_2|\mathbf{r}_3|\mathbf{r}_+\right]. \tag{A.12}$$

The corresponding left eigenvectors are:

$$\mathbf{l}_{\mp} = \left(\pm\frac{h^2}{\Delta}\right)\begin{bmatrix} hW\mathcal{A}_{\pm}\left(v^x - \lambda_{\pm}\right) - v^x - W^2\left(v^2 - v^x v^x\right)\left(2\mathcal{K} - 1\right)\left(v^x - \mathcal{A}_{\pm}\lambda_{\pm}\right) + \mathcal{K}\mathcal{A}_{\pm}\lambda_{\pm} \\ 1 + W^2\left(v^2 - v^x v^x\right)\left(2\mathcal{K} - 1\right)\left(1 - \mathcal{A}_{\pm}\right) - \mathcal{K}\mathcal{A}_{\pm} \\ W^2 v^y\left(2\mathcal{K} - 1\right)\mathcal{A}_{\pm}\left(v^x - \lambda_{\pm}\right) \\ W^2 v^z\left(2\mathcal{K} - 1\right)\mathcal{A}_{\pm}\left(v^x - \lambda_{\pm}\right) \\ -v^x - W^2\left(v^2 - v^x v^x\right)\left(2\mathcal{K} - 1\right)\left(v^x - \mathcal{A}_{\pm}\lambda_{\pm}\right) + \mathcal{K}\mathcal{A}_{\pm}\lambda_{\pm} \end{bmatrix}, \tag{A.13}$$

with

$$\Delta = h^3 W\left(\mathcal{K} - 1\right)\left(1 - v^x v^x\right)\left(\mathcal{A}_+\lambda_+ - \mathcal{A}_-\lambda_-\right), \tag{A.14}$$

the determinant of the matrix of the right eigenvectors $\mathbf{R}$.

$$\mathbf{l}_1 = \frac{W}{\mathcal{K} - 1}\left(h - W, Wv^x, Wv^y, Wv^z, -W\right), \tag{A.15}$$

$$\mathbf{l}_2 = \frac{1}{h\left(1 - v^x v^x\right)}\left(-v^y, v^x v^y, 1 - v^x v^x, 0, -v^y\right), \tag{A.16}$$

$$\mathbf{l}_3 = \frac{1}{h\left(1 - v^x v^x\right)}\left(-v^z, v^x v^z, 0, 1 - v^x v^x, -v^z\right) \tag{A.17}$$

These eigenvectors are the rows of the matrix

$$\mathbf{R}^{-1} = \left[\mathbf{l}_-, \mathbf{l}_1, \mathbf{l}_2, \mathbf{l}_3, \mathbf{l}_+\right]. \tag{A.18}$$

Appendix B

The Newton-Raphson algorithm for recovering the primitive variables

We use the procedure of Martí et al. [37] for the recovering of the primitive variables. The primitive variables $w = (\rho, v^i, p)$ are computed from the conserved ones

$$\mathbf{U} = \begin{pmatrix} D \\ M^i \\ \tau \end{pmatrix} = \begin{pmatrix} \rho W \\ \rho h W^2 v^i \\ \rho h W^2 - p - D \end{pmatrix}, \tag{B.1}$$

by solving the implicit equation

$$f(p) = (\gamma - 1)\rho_* \epsilon_* - p = 0 \ , \tag{B.2}$$

by the one-dimensional Newton-Raphson algorithm

$$\frac{\partial f^n(p)}{\partial p} \delta p^{n+1} = f^n(p) \, . \tag{B.3}$$

The variables ρ_* and ϵ_* are given by

$$\rho_* = \frac{D}{W_*} \tag{B.4}$$

and

$$\epsilon_* = \frac{\tau + D(1 - W_*) + p(1 - W_*^2)}{D W_*} \ , \tag{B.5}$$

where the Lorentz factor is given by

$$W_* = \frac{1}{\sqrt{1 - g_{ij} v_*^j v_*^j}} \tag{B.6}$$

and the velocity components are

$$v_*^j = \frac{M^j}{\tau + D + p}. \tag{B.7}$$

Since the value of the velocity is limited by the speed of light, $|v| < 1$, there exists a lower bound of the pressure

$$p_{min} = \sqrt{g_{ij} M^j M^j} - (\tau + D). \tag{B.8}$$

Therefore, the physical value of the pressure has to be in the physically allowed range $p \in]p_{min}, \infty[$ and the zero of $f(p)$ in this range determines the pressure. The absolute value of velocity is computed directly from equation (B.7) and the remaining primitive variables ρ, v^i are computed from equations (B.1) and from the definition of the Lorentz factor W. The Jacobian $f'(p)$ of the function $f(p)$ is approximated by

$$f' \approx v_*^2 c_{s*}^2 - 1, \tag{B.9}$$

where c_{s*} is the sound speed

$$c_{s*} = \sqrt{\frac{(\gamma - 1)\gamma\epsilon_*}{1 + \gamma\epsilon}}. \tag{B.10}$$

Bibliography

[1] M. Aloy, J. Ibáñez, J. Martí, and E. Müller. Technical Report MPA 1123, MAX-PLANCK-INSTITUT FÜR ASTROPHYSIK, NOV 1998.

[2] R. Arnowitt, S. Deser, and C. Misner. In L. Witten, editor, *Gravitation: An introduction to current research*. Whiley, New York, 1962.

[3] H. Atkins and C. Shu. *AIAA Journal*, 36:775–782, 1998.

[4] F. Banyuls, J. Font, J. Ibáñez, J. Martí, and J. Miralles. *ApJ*, 476:221–231, 1997.

[5] F. Bassi and S. Rebay. In B. Cockburn, G. Karniadakis, and C.-W. Shu, editors, *Discontinuous Galerkin Methods*, volume 11 of *Lecture Notes in Computational Science and Engineering*, pages 197–208. Springer, 2000.

[6] F. Bassi, S. Rebay, and C. Shu. *J. Comp. Phys.*, 131:267–279, 1997.

[7] S. Bonazzola, E. Gourgoulhon, and J.-A. Marck. Sissa e-Print: grqc/9811089, 1998.

[8] J. Boris and D. Book. *J. Comp. Phys.*, 11:38–69, 1973.

[9] M. Camenzind. *A&A*, 156:137–151, 1986.

[10] S. Chakrabarti and R. Khanna. *Mon. Not. Roy. Astron. Soc.*, 256:300–306, 1992.

[11] B. Cockburn, S. Hou, and C. Shu. *Math. Comp.*, 54:545–581, 1990.

[12] B. Cockburn, G. Karniadakis, and C.-W. Shu, editors. *Discontinuous Galerkin Methods*, volume 11 of *Lecture Notes in Computational Science and Engineering*. Springer, 2000.

[13] B. Cockburn and C. Shu. *J. Comp. Phys.*, 141:199–224, 1998.

[14] B. Cockburn and C. Shu. *SIAM J. Numer.Ana.*, 35:2440–2463, 1998.

[15] P. Colella and P. Woodward. *J. Comp. Phys.*, 54:174–201, 1984.

[16] R. Donat, J. Font, J. Ibáñez, and A. Marquina. *J. Comp. Phys*, 146:58, 1998.

[17] R. Donat and A. Marquina. *J. Comp. Phys.*, 125:42–58, 1996.

[18] G. Duncan and P. Hughes. *ApJ*, 436:L119, 1994.

[19] C. Evans and J. Hawley. *ApJ*, 332:659–677, 1988.

[20] J. Font. in: Living rev. relativity, 2. http://www.livingreviews.org/Articles/Volume2/2000-2font, 2000.

[21] J. Hawley. *ApJ*, 381:496–507, 1991.

[22] J. Hawley, L. Smarr, and J. Wilson. *ApJ*, 277:296–311, 1984.

[23] J. Hawley, L. Smarr, and J. Wilson. *ApJ Suppl. Ser.*, 55:211–246, 1984.

[24] P. Hughes and G. Duncan. *Bull. of the Am. Astro. Soc.*, 26:928, 1994.

[25] P. Hughes, M. Miller, and G. Duncan. *Bull. of the Am. Astro. Soc.*, 30:1250, 1998.

[26] I. Igumenshchev and A. Belodorov. *Mon. Not. Roy. Astron. Soc.*, 284:767–772, 1997.

[27] R. Khanna and M. Camenzind. *A&A*, 307:665–685, 1996.

[28] S. Koide, J.-I. Sakai, K.-I. Nichikawa, and R. Mutel. *ApJ*, 464:724, 1996.

[29] S. Koide, P. Shibata, and T. Kudoh. *ApJ*, 495:L63–L66, 1998.

[30] S. Koide, P. Shibata, and T. Kudoh. *ApJ*, 522:727–752, 1999.

[31] S. Komissarov. *Mon. Not. Roy. Astron. Soc.*, 303:343–366, 1999.

[32] S. Komissarov and S. Falle. In P. Hardee, A. Bridle, and J. Zensus, editors, *Energy Transport in Radio Galaxies and Quasars*, page 173. San Francisco: ASP, 1996.

[33] S. Komissarov and S. Falle. *Mon. Not. Roy. Astron. Soc.*, 288:833–848, 1997.

[34] S. Komissarov and S. Falle. *Mon. Not. Roy. Astron. Soc.*, 297:1087–1108, 1998.

[35] M. Krause and M. Camenzind. *A&A*, 380:789–804, 2001.

[36] R. LeVeque. In O. Steiner and A. Gautschy, editors, *Computational Methods for Astrophysical Fluid Flows*, volume 27 of *Saas-Fee Advanced Course*, pages 1–159. Springer, 1997.

[37] J. Martí, J. Ibáñez, and J. Miralles. *Phys. Rev. D*, 43:3794–3801, 1991.

[38] J. Martí and E. Müller. *J. Fluid Mech.*, 258:317, 1997.

[39] J. Martí and E. Müller. in: Living rev. relativity 3. 1999.

[40] J. Martí, E. Müller, J. Font, and J. Ibáñez. *ApJ Lett.*, 448:L105, 1995.

[41] J. Martí, E. Müller, J. Font, J. Ibáñez, and A. Marquina. *ApJ*, 479:151–163, 1997.

[42] D. Meier. e-Print: arXiv/astrp-ph/9806278 v2, 1998.

[43] C. Misner, K. Thorne, and J. Wheeler. *Gravitation.* Freemann, San Francisco, 1973.

[44] K.-I. Nichikawa. *ApJ*, 483:L45, 1997.

[45] K.-I. Nichikawa. *ApJ*, 498:166, 1998.

[46] T. Oden and C. Baumann. In B. Cockburn, G. Karniadakis, and C.-W. Shu, editors, *Discontinuous Galerkin Methods*, volume 11 of *Lecture Notes in Computational Science and Engineering*, pages 179–196. Springer, 2000.

[47] B. Paczyński and P. Wiita. *A&A*, 88:23–31, 1980.

[48] P. Papadopoulos and J. Font. *Phys. Rev. D*, 58:1–9, 1998.

[49] J. Peitz and S. Appl. *Mon. Not. Roy. Astron. Soc.*, 296:231–244, 1998.

[50] W. Reed and T. Hill. Technical Report LA-UR-73-479, Los Alamos Scientific Laboratory, 1973.

[51] A. Rosen, P. Hughes, G. Duncan, and P. Hardee. *ApJ*, 516:729, 1999.

[52] N. Shakura and R. Sunyaev. *A&A*, 24:337–355, 1973.

[53] C. Shu and S. Osher. *J. Comp. Phys.*, 77:439–471, 1988.

[54] C. Shu and S. Osher. *J. Comp. Phys.*, 83:32–78, 1989.

[55] J. Steger and R. Warming. *J. Comp. Phys.*, 40:263, 1981.

[56] J. Stone and M. Norman. *ApJ. Supp. Ser.*, 80:753–790, 1992.

[57] M. van Putten. *ApJ Lett.*, 408:L21, 1993.

[58] M. van Putten. *ApJ Lett.*, 467:L57, 1996.

[59] T. Warburton and G. Karniadakis. *J. Comp. Phys.*, 152:1–34, 1999.

[60] J. Wilson. *ApJ*, 173:431–438, 1972.

[61] P. Woodward and P. Colella. *J. Comp. Phys.*, 54:115–173, 1984.

[62] M. Yokosava. *Publ. Not. Astron. Soc. Japan*, 45:207–218, 1993.

[63] M. Yokosava. *Publ. Not. Astron. Soc. Japan*, 47:605–615, 1995.

[64] U. Ziegler and H. York. *Comp. Phys. Comm.*, 101:54, 1997.

Ein herzliches Dankeschön an ...

...Max Camenzind, für seine kompetente Betreuung dieser Arbeit, für seine Geduld mit mir und für die durch ihn vermittelte Einsicht, dass herum "simulieren" und "schöne" Bildchen produzieren ein physikalisches Verständnis nicht ersetzen können.

...Ramon Khanna[1], für seine Unterstützung und Einführung in die Gebiete der Finiten Elemente und für die Erläuterung was denn da so passiert in der Nähe von Schwarzen Löchern (FIDOs=Pudel?). Desweiteren für seinen Humor und natürlich für seine "Workshops" der bizarren Art.

...Andreas Burkert, für sein Interesse an dieser Arbeit und der Erstellung des Zweitgutachtens.

...Jochen Peitz[1,2], für Diskussionen physikalischer und sonstiger Art zu später Stunde unter dem Einfluss extremer Umweltbedingungen (CAVE 54, Sneak Preview).

...Stefan Appl[1], für seinen Durchblick, kritischen Fragen und aufmunternde Art wenn mal wieder gar nichts funktionierte.

...Jose Gracia[1], für die schnelle Hilfe bei Problemen mit Linux und für Diskussionen über das "seltsame" Verhalten zeitabhängiger Akkretionsscheiben (was ist hier physikalisch und was ist da nur numerisches Artefakt).

... den Ehemaligen und Mitgliedern der Theorie-Gruppe[1](Elena Breitmoser, Markus Thiele, Martin Krause, Andreas Müller, Matthias Stute) und der Sternwarte für die freundliche Arbeitsatmosphäre.

...der Sneak Preview Gruppe[2], Markus Feldt[2,3], a.D. Jochen Peitz, Michael Reuter und Thomas Wagner, für das gemeinsame Ertragen dieser "Meisterwerke der Filmgeschichte" und nachfolgender Erörterung derselben.

...dem "Stammtisch[3]", Holger Bock, Anke Heines und Sascha Kempf[2,3] samt Kinder, sowie Denise und Marek, für so manchen schönen Abend inklusive Papierflieger basteln.

...meinen Eltern und meinem Bruder, für ihr reges Interesse und Unterstützung jeglicher Art.

... und natürlich meiner Freundin Annette Kritzer[2,3] für alles was das Leben lebenswert macht.